SVEUČILIŠTE U SPLITU
FAKULTET ELEKTROTEHNIKE, STROGARSTVA I BRODOGRADNJE

POSLIJEDIPLOMSKI DOKTORSKI STUDIJ ELECTROTEHNIKE I INFORMACIJSKE TEHNOLOGIJE

KVALIFIKACIJSKI ISPIT

SIGNAL PROCESSING IN DIAMOND BASED NEUTRON DETECTORS AT CRYOGENIC TEMPERATURES

Donny Domagoj Cosic

Split, srpanj 2022

CONTENTS

1. INTRODUCTION

In the past decade there have been many significant advances in fusion research, most notably with the construction commencement of the International Thermonuclear Experimental Reactor (ITER). Outlined in [1], ITER is a key facility in the European roadmap towards fusion electricity and a stepping stone towards the Demonstration power plant (DEMO). However, the step between ITER and DEMO is quite large with many issues still unresolved. One of these issues is the effects of neutrons generated by fusion on materials in the immediate surrounding of the reactor core. To study this issue in more details, a dedicated International Fusion Material Irradiation Facility – DEMO Oriented Neutron Source (IFMIF – DONES) is being constructed to produce a similar neutron environment as expected in DEMO for material research. The DONES design is based on a superconductive accelerator which will accelerate deuterium ions to 40 MeV with a beam current of 125 mA onto a liquid lithium target to produce a neutron fluence of 10^{18} n/m^2/s [2]. Due to the high beam power (5 MW), the importance and requirements of the beam diagnostic systems become crucial for the operation of the accelerator and personnel safety.

Micro-loss (μ-loss) monitors or beam loss monitors (BLM) are part of this diagnostic system and are required to trigger the Machine Protection System in case of beam loss. μBLM should be able to monitor beam losses down to 1 W/m (or 10^{-6} of the total beam power) and be used for fine tuning the accelerator during normal operation [3], [4]. To satisfy all three requirements, the detector must be mounted as close as possible to the beam, placing additional requirements on the detector [5]:

- High radiation tolerance
- Stability at cryogenic temperatures
- Fast response time
- High sensitivity to neutrons and lower sensitivity to γ-rays

Radiation detectors based on diamonds fulfill these requirements due to their size, physical and electrical properties. Gamma radiation is detected through three interaction mechanism: Photoelectric absorption, Compton scattering and Pair production. Out of these three interaction methods, photoelectric absorption and Compton scattering are the most probable for lower energy gamma rays. Where the probability of the photoelectric effect scales with Z^{3-4} and linearly with Z for Compton scattering and its sensitivity is proportional to the Z number of the element. Diamond

is the least sensitive solid-state detector to gamma radiation. Low Z materials have also the additional benefit to be more radiation resistant to high energy particles because nuclear fragments are light and cause a small amount of non-ionizing energy loss inside the material [6]. Further radiation hardness comes from the high displacement energy required to move a carbon atom out of its lattice position, decreasing the number of vacancies created and therefore creating less traps for charge carriers. Due to these properties, the European Organization for Nuclear Research (CERN) created a dedicated research group (RD42) to investigate diamond based detectors for future large hardon colliders [7]–[9][10]. To achieve fast response times from in the detector, it is desirable to have the charge carrier velocity as large as possible. This is accomplished by increasing the electric field across the device until the charge carrier velocities reach saturation. The large dielectric strength of diamond allows for very large bias voltages to be applied without causing breakdown. Typical bias voltages applied to diamond detectors are in the range of 1 V/μm or higher, which for a 300 μm diamond equals to 300 V. Furthermore, at these high bias levels, the leakage current through the device is still in the order of pico- to nanoamps due to the low intrinsic resistance of diamond. This low leakage current results in very low noise from the detector [11].

2. INTERACTION OF RADIATION WITH MATTER

In order to understand how a diamond can be used as a radiation detector, it is important to understand how radiation interacts with matter. The interaction mechanism of radiation with the detector depends on the type of radiation, more specifically, is the radiation in the form of charged particles (ions, electrons) or neutral particles. Charged particles loose energy through direct electric field interactions which can be detected. While neutral particles first have to transfer their energy to charged particles inside the matter through collisions or nuclear reactions which can then be detected. The amount of energy a particle loses in matter is quantified by means of macroscopic and microscopic interaction cross sections. Macroscopic cross section is defined as the linear attenuation coefficient which describes the interaction probability per unit path length. Microscopic cross section is defined as the effective cross-sectional area of the matter to the incident particle for a given interaction mechanism and is usually presented in Barn units, 1 barn is equal to 10^{-28} m^2 [12].

2.1. Ionizing radiation

Ionizing radiation interacts with the detector predominantly through the coulomb force between the electrons of the detector material and the incident particle. The energy transfer from the impeding ion to electrons in the material is small, therefore many collisions are required before the ion loses all of its energy resulting in a trail of ionization along its trajectory [13]. For heavy charged particles this mean energy loss, or stopping power, is described by the Bethe equation or more generally by the Bethe-Bloch equation and is valid over a larger energy range. The Bethe-Bloch equation with the low energy correction is presented below in equation 2.1:

$$-\frac{dE}{dx} = \frac{4\pi e^4 z^2}{m_0 v^2} NZ \left[\ln\left(\frac{2m_0 v^2}{I}\right) - \ln\left(1 - \frac{v^2}{c^2}\right) - \frac{v^2}{c^2} \right] \tag{2.1}$$

where v is the velocity and z is the charge of the primary particle, N is the number density, Z is the atomic number and I is the average ionization energy of the detector material, m_o is the electron rest mass and e is the electron charge. Note that for nonrelativistic particles where $v << c$, the last two term of the equation can be discarded [14]. From the Bethe-Bloch equation 2.1, it can be concluded that the energy loss is inversely proportional to the impeding ion velocity. Therefore,

most of the ion energy is deposited at the end of its trajectory inside the detector resulting in a Bragg peak after which there is no more ionization. This phenomenon is illustrated in Figure 2.1 for 5.5 MeV alpha particles in diamond using the Stopping and Range of Ions in Matter simulation software (SRIM) which calculates the ionization profile using the Monte Carlo technique [15]. The width of the Bragg peak is a result of energy straggling which is caused by the energy loss being a statistical or stochastic process where not all particles transverse the same path in the material.

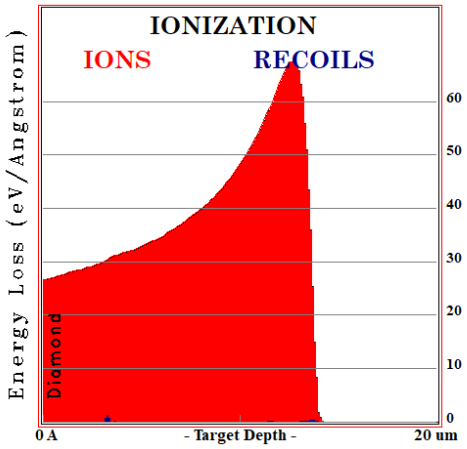

Figure 2.1 - Ionization profile of 5.5 MeV alpha particles in Diamond

The above equation is only valid for heavy ions and must be modified for lighter particles such as electrons. Fast electrons lose a larger fraction of energy with each collision and have larger deviation in their trajectories due their mass being equal to the electrons in the material. Additionally, electrons lose a significant portion of their energy through radiative process along with coulomb interactions. Radiative process such as bremsstrahlung or electromagnetic radiation which is emitting when any charged particle accelerates. The amount of energy loss through bremsstrahlung depends greatly on the Z number of the detector material and increases as size of the atoms in the detector material increase [16].

Photons, such as the those created by bremsstrahlung, transfer their energy to the electrons in the detector material predominantly through three mechanisms: photoelectric effect, Compton scattering and pair production. The energy transfer can be partial or complete and greatly depends on the energy of the incoming photon. The photoelectric effect dominates for lower photon energies, where the photon energy is completely absorbed in the process of ejecting an electron from the inner atomic shells (usually the K shell) of an atom. The ionized atom consequently fills

this vacancy by capturing a free electron or rearranging electrons from other shells. Relocation of electrons from outer shells to the K shell results in the emission of an X-ray photon. The atom can also de-excite through the emission of an electron from the outer shell. These emitted electrons are called Auger electrons [14], [16]. At intermediate photon energies, the Compton effect dominates where the incident photon is scattered off an electron, recoiling the electron and resulting in the emission of a lower energy photon. Furthermore, if the incident phonon energy is more than twice the rest mass energy on an electron (1.02 MeV), pair production is possible. Pair production converts the photon energy into the creating on an electron-position pair with all the energy above 1.02 MeV transferred equally to the kinetic energy of the created particles. Consequently, the position annihilates with an electron resulting in the emission of two 511 keV gamma rays emitted in opposite directions to conserve momentum.

2.2. Nonionizing radiation

Neutrons carry no charge and therefore cannot interact with the detector directly through the coulomb force as is the case for ionizing radiation. Neutrons interact almost exclusively with the nucleus of an atom through two scattering mechanisms. Capture scattering results when the neutron is absorbed by the detector material nucleus to form a compound nucleus. If the compound nucleus is left in the ground state, the scattering is elastic. In elastic scattering, the incident neutron transfers a portion of its energy to the atom (E_R), which can be calculated by scattering theory; $E_R = \frac{4AE_n}{(1+A)^2}$ where E_n is the neutron energy and A is the mass of the material nucleus. In a diamond detector, a 1 MeV neutron will transfer 0.284 MeV of energy to a carbon atom, about 28 % of its energy [17]. However, if the compound nucleus is left in an excited state, the scattering is inelastic. Potential scattering, on the other hand, is always elastic where the incident neutron is scattered by the nucleus of an atom in the detector [12]. The probability of the type of reaction is heavily depended on the incident neutron energy. This probability per unit path length is constant for a fixed neutron energy and is expressed in terms of cross section in units of the barn. Neutron cross sections are empirically derived through experiments and generally exhibit resonance behavior. Databases of cross sections are available online through the International Atomic Energy Agency's (IAEA) on their Experimental Nuclear Reaction Data (EXFOR) [18] and through the National Nuclear Data Center's (NNDC) Nudat [19]. Interactions are commonly divided into two groups, slow and fast

neutrons interactions with fast neutrons being anything above 0.5 eV (the cadmium cutoff energy) [14].

2.2.1. Fast neutrons

In general, nuclear reaction cross sections decrease with energy and scattering becomes the dominant neutron energy transfer mechanism. Due to the mass of a neutron, a significant amount of energy can be transferred in a single collision. These collisions displace atoms in the detector which produces a detectable signal. After each collision, neutrons lose energy to become slow neutrons in a process known as neutron moderation. Moderation is widely used in nuclear reactors to bring the neutron energy down to favorable levels for nuclear reactions. However, in some elements, nuclear capture channels open only at higher energy levels allowing for nuclear reactions to take place only with fast neutrons. In the context of this paper, we will focus on diamond, that is on carbon for which nuclear reactions are only possible for neutrons of higher energy. Table 2.1 summarized most common neutron induced nuclear reactions in carbon, however many more reactions with carbon exist [20].

Table 2.1 - Neutron induced reaction in carbon

Reaction	**Q-Value [MeV]**	**E_{th} [MeV]**
$^{13}C(n,\alpha)^{10}Be$	3.836	4.134
$^{12}C(n,\alpha)^{9}Be$	5.702	6.182
$^{12}C(n,n+2\alpha)^{4}He$	7.275	7.886
$^{12}C(n,p)^{12}B$	12.587	13.645
$^{12}C(n,d)^{11}B$	13.732	14.887

The Q value in Table 2.1 depicts the energy absorbed in the (exothermic) reaction while the E_{th} represents the threshold energy at which such a reaction can occur. Using the Q value and a kinematic calculator (such as CATKIN [21]), the expected energy of the nuclear reaction products can be calculated. Taking the reaction of a neutron with ^{12}C, $E_n - 5.702 = E_\alpha + E_{Be}$. As will be later demonstrated, this is the key principle in detection of neutrons based on secondary products [22]. The reaction threshold energy (E_{th}) can be observed for the $^{12}C(n,\alpha)^{9}Be$ reaction in cross section data as illustrated by the grey line in Figure 2.2. The figure additionally contains the total, elastic, inelastic and (n,α) reaction cross section information for ^{12}C in barns for incident neutrons in the

energy range of $0.5 < E_n < 20$ MeV. As can be observed from the figure, the alpha channel (grey line) opens at 6.182 MeV and peaks below 10 MeV.

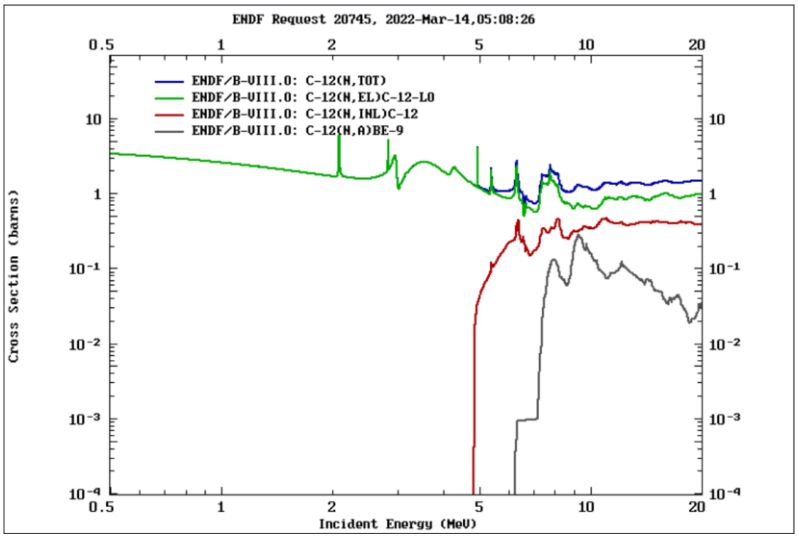

Figure 2.2 - Neutron cross section for ^{12}C [18]

2.2.2. Slow neutrons

In contrast to fast neutrons, very little energy is transferred by slow neutrons through elastic scattering, and they do not displace the atoms in the material by a detectable amount. These collisions eventually bring the neutron into thermal equilibrium with the material, which at room temperature is 0.025 eV. As depicted in Table 2.1, slow neutrons are not directly detectable with a diamond detector and a converter layer must be introduced to detect them. Most commonly a thin layer of ^{6}Li or ^{10}B is placed before the diamond detector to convert the neutron into other ionized particles. The associated reactions and Q-values are summarized in Table 2.2, along with their cross sections in Figure 2.3.

Table 2.2 - Converter layer reactions for the detection of slow neutrons with a diamond detector

Reaction	Q-Value [MeV]	Product Energy [MeV]
$^{6}Li(n,\alpha)^{3}H$	4.79 [23]	$E_\alpha = 2.06$, $E_T = 2.73$
$^{10}B(n,\alpha)^{7}Li$	2.792 [24]	$E_\alpha = 1.47$, $E_T = 0.84$

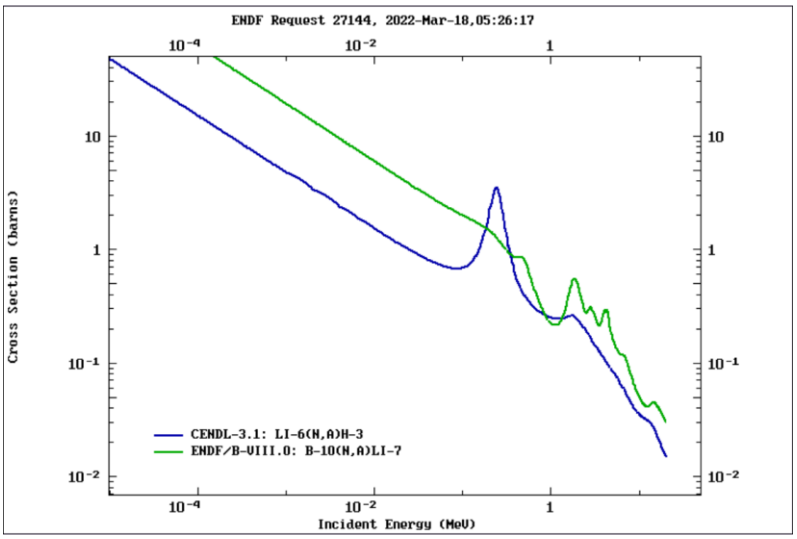

Figure 2.3 - Neutron cross section data for ^{6}Li and ^{10}B [18]

Both reactions release an alpha particle along with an ion which can be detected with the diamond detector. As is the case for fast neutrons, the energy of these secondary particles can be calculated using the Q-value of the reaction and a kinematics calculator. Additionally, from Figure 2.3 it can be observed that the reaction probability (cross section) is an order of magnitude higher than for the $^{12}C(n,\alpha)^{9}Be$ for neutron energies under 1 MeV. Out of the two converters, ^{6}Li is preferred even though it has a lower cross section, because of the high Q-values of the reaction. This high Q-value means that the reaction products have a larger kinetic energy making them easier to detect in the diamond and less sensitive to the converter layer thickness. Typical energies of the alpha particle generated from the ^{10}B and ^{6}Li are 1.47 MeV and 2.06 MeV, respectively resulting in a penetrating depth of 7.8 μm in B_2O_3 and 19.5 μm in LiF [25].

2.3. Neutron generation

In order to perform experiments with neutrons, a stable, preferably monoenergetic source of neutrons of appropriate energy are required. In this section, we will briefly outline the most common methods of generating neutrons for experiments as it is important to understand the reactions involved to correctly interpret spectrum data obtained from the detector. Neutron sources are divided into two categories, radioisotope sources and accelerator reaction based sources. Both types of sources release an array of secondary products along with a neutron in the form of gamma, x-ray radiation as well as other ions which are used to calculate the neutron flux but also add a

significant background to the detector being tested. Table 2.3 summarizes applicable neutron sources for this work [26]. Furthermore, for simulating a fusion environment, Deuterium-Deuterium (D-D) and Tritium-Deuterium (T-D) are used, as the majority of fusion devices are based on these reactions [25].

Table 2.3 - Neutron source reactions

	Neutron Energy [MeV]	**Properties**
Radioisotopes		
^{252}Cf	2.1	Average energy - Broad spectrum neutrons
$^{241}Am^{9}Be$	4.2	
Accelerator induced reactions		
$^{7}Li(p,n)^{7}Be$	0.2 – 0.7	Monoenergetic - Neutron energy based on primary ion energy
$^{3}H(p,n)^{3}He$	0.7 – 3	
$^{2}H(^{2}H,n)^{3}He$ (D-D)	3.5 – 8	
$^{3}H(p,n)^{3}He$	3 – 13	
$^{3}H(^{2}H,n)^{4}He$ (T-D)	14 – 20	

3. RADIATION DETECTION WITH DIAMONDS

A typical diamond detector is composed of a diamond sandwiched between two coplanar electrodes on each side and operates as a solid-state ionization chamber [27]. Unlike narrow-band semiconductors where a PN-junction must be fabricated by doping to form a sensitive volume with low charge carrier concentrations, diamond is a wide-band semiconductor, and it intrinsically contains low charge carrier concentrations. Therefore, the sensitive volume is defined by the size of the electrodes and the thickness of the diamond. Charged particles produce electron-hole pairs in the detector by promoting electrons from the valence band into the conduction band. If no external electric field is present, the free charge carriers drift in random directions with a thermal velocity. However, if an external field is applied across the diamond by placing a large potential difference between the electrodes, the generated charge carriers then drift towards the electrodes under the influence of this external electric field, pushed by the Lorentz force. The number of e-h pairs generated is proportional to the deposited energy from the charged particle and can be calculated by dividing the deposited energy by the average energy required to generate an e-h pair (E_{pair}), which in diamond is approximately 13.6 eV [28]. However this is only true if the carrier lifetime is much larger than the carrier drift time [29]. Charge carrier mobility is affected by many factors such as the purity of the crystal lattice (the amount of defects), temperature and will be discussed in detail in the following section.

The properties of diamond compared to silicon and germanium are summarized in Table 3.1. These values vary in literature and are therefore presented here in a range [3], [5], [28]–[31]. Additionally, the last column in Table 3.1 highlight how the specific properties benefit a detector based on diamond.

Table 3.1 - Detector properties

	Diamond	**Silicon**	**Germanium**	**Diamond Advantage**
Atomic Number (Z)	6	14	32	Radiation hardness
Bandgap [eV]	5.48	1.12	0.67	Lower noise
Dielectric strength [V/cm]	10^7	$3 \cdot 10^5$	10^5	Large bias
Intrinsic resistivity [Ω/cm]	up to 10^{16}	$2.3 \cdot 10^5$	50	Lower leakage current
Electron mobility [cm^2/Vs]	1300 - 4500	1350	3900	Fast response
Hole mobility [cm^2/Vs]	1800 - 3800	480	1900	Fast response

Electron lifetime [s]	10^{-10} - 10^{-6}	> 10^{-3}	> 10^{-3}	Better charge collection
Hole lifetime [s]	10^{-10} - 10^{-6}	10^{-3}	$2 \cdot 10^{-3}$	Better charge collection
Dielectric constant	5.72	11.9	16	Low capacitance
Displacement energy [eV]	43	13 - 20	28	Radiation hardness
Energy to create e-h pair [eV]	11.1 - 24	3.62	2.96	Disadvantage - lower output signal

The large range of values reported in Table 3.1 results from variations in the quality of diamonds used for detectors. Most of the highest quality diamonds are manufactured using the chemical vapor deposition (CVD) method, where a diamond is grown layer by layer from a seed. Using this method single crystal CVD (scCVD) or polycrystalline (pCVD) can be manufactured. scCVD diamonds are preferred for detector use since they have no grain boundaries resulting in fewer traps for charge carriers. This improves the charge collection efficiency and output signal amplitude up to a factor of 3 in comparison to pCVD diamonds [6]. Electronic grade scCVD diamonds have less than 5 ppb of nitrogen and boron impurities. However, they are significantly more expensive, and their size is limited to approximately 4 x 4 mm. pCVD diamonds are not limited in size, cheaper to manufacture and therefore preferred in some applications where a larger detector is required.

Furthermore, as depicted in Table 3.1, the energy required to lift an electron into the conduction band, the bandgap energy (E_g), is 5.47 eV while the average energy required to create an e-h pair is much higher. This is due to non-ionizing energy losses as a portion of the incident particle energy goes into the creation of phonons.

$$E_0 = E_{ph}N_{ph} + E_gN_i \tag{4.1}$$

E_{ph} and N_{ph} represent the average phonon energy and number of photons, respectively while E_g is the bandgap and N_i is the number of e-h pairs created. Therefore, approximately 8 eV (60 % of the energy) goes into the creation of phonons. A further benefit of the relatively large bandgap energy of diamond compared to silicon (1.12 eV), is a lower noise in the signal from the detector due insufficient thermal energy at room temperature to generate electron hole pairs.

Furthermore, with the incident energy being fixed, equation (4.1) can be rewriting in terms of the fluctuation in the number of phonons and e-h pairs as follows [30]:

$$E_g \Delta N_i = E_{ph} \Delta N_{ph} \tag{4.2}$$

thus, over many events the variance in the number of e-h pairs, which is the intrinsic resolution of the detector, can be written as

$$\sigma_Q = \sqrt{F \frac{E_0}{E_{pair}}} \tag{4.3}$$

where F is known as the Fano factor. The Fano factor ranges from 0.08 to 0.14 for semiconductor materials. There is no reliable experimental data for the diamond Fano factor, but it has been theoretically predicted to be 0.08. The Fano factor for silicon is 0.115 [29], [32].

The generated charge carriers drift through the material with a drift velocity which is proportional to the electric field strength (E). This proportionality constant is defined as the mobility (μ) and has units of cm^2/Vs. Theoretically, the drift velocity can increase indefinitely with increasing electric field strength, however in practice there is a limit to the maximum drift velocity due to increased phonon scattering. This maximum drift velocity is known as the saturation velocity. Considering the saturation velocity (v_s), the drift velocity (v_{dr}) is expressed as a function of the low field mobility (μ_0) as [33]:

$$v_{dr} = \frac{\mu_0 E}{1 + \frac{\mu_0 E}{v_s}} \tag{4.4}$$

however, this is only an approximation for ideal conditions such as infinite coplanar electrodes. The real drift velocity is position depended since the electric field is depended on the detector electrode configuration. The general drift velocity can be obtained by the differential equation $\frac{dx}{dt} = \mu(E)E(x)$. As is the case with charge carrier mobility values in diamond (Table 3.1), saturation

velocity also vary in literature and is in the range of 1.2 x 10^5 m/s to 9.6 x 10^5 m/s and 1.2 x 10^5 to 14.1 x 10^5 m/s for electrons and holes, respectively [28], [33].

As the charge carriers move inside the diamond under the influence of the electric field, they induce current in the electrodes of the detector as described by the Shockley-Ramo theorem [34]. Shockley-Ramo showed that the current on the electrode is the sum of the electrostatic influence of the charges at each moment as they drift inside the diamond. The resulting current on the detector electrode is described by the following equation simplified for the case of a detector configured as a parallel plate capacitor.

$$I = q\frac{v_{dr}}{d} \tag{4.5}$$

q is the charge of the electron and d is the thickness of the detector. The drift velocity can be also simplified to $v_{dr} = \mu E$ from equation (4.4) by disregarding the saturation velocity, resulting in an expression for the current from the detector:

$$I = q\frac{\mu E}{d} \tag{4.6}$$

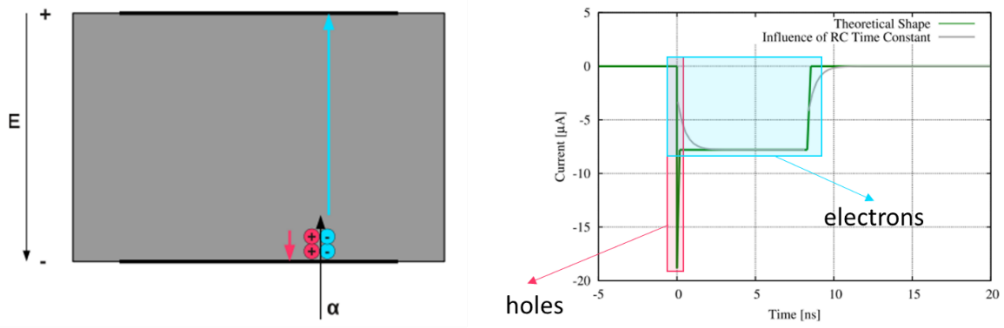

Figure 3.1 - Induced current from an Alpha particle [28], [30]

The induced current is the superposition of the contribution of electrons and holes as they drift towards opposite electrodes. Figure 3.1 illustrates the induced current resulting from an alpha particle impinging a diamond detector with coplanar electrodes. The decay of ^{241}Am produces an alpha particle with energy of 5.5 MeV which penetrates 14 μm into diamond [15]. This produces

on average 4.04 x 10^5 e-h pairs using the average energy required to create an e-h pair (E_{pair}) to be 13.6 eV as stated above, corresponding to 65 fC of charge deposited in the diamond.

$$Q_0 = \frac{qE_\alpha}{E_{pair}} = 65\ fC \tag{4.7}$$

$$N_{eh} = \frac{E_\alpha}{E_{pair}} = 4.04x10^5 \tag{4.8}$$

The generated electrons have to transverse the full thickness of the diamond to reach the positive electrode, while generated holes travel only 14 μm to reach the negative electrode. For a typical thickness of a diamond detector of 500 μm and 1 V/μm electric field the maximum transit time is:

Table 3.2 - Transit time for charge carriers

	v_{dr} [m/s]	d [μm]	t [ns]
Electrons	6x10^4	500	8.3
Holes	8.5x10^4	14	0.165

From the graph on the right of Figure 3.1, the influence of each charge carrier can be observed on the total induced current on the electrodes. The short transit time for holes (165 ps) results in a current spike while electrons travel 8.3 ns through the bulk of the diamond detector to reach the other electrode. The current from the electrons $I_e = \frac{Q_e}{t} = 7.8\ \mu A$ which, when measured through a 50 Ω based system, results in a 0.4 mV signal. Furthermore, not all the charge is instantaneously accelerated towards the electrodes as the outer charge carriers in the generated charge cloud screen the inner charge carriers from the electric field. This affects the rise time of the current pulse as not all the charge carriers reach the drift velocity at the same time. This effect is compounded by the RC constant of the system which limits the bandwidth, causing the hole contribution to be difficult to observe resulting in a signal depicted by the gray curve in Figure 3.1 [28]. This will be further discussed later in this work.

An alpha particle of sufficiently low energy to stop inside the volume of the detector was used to illustrate the basic principle of charge generation and collection inside a diamond detector.

However, the resulting current profiles are very different for minimum ionizing particles (MIPs) which transvers the whole volume of the detector and do not stop in the detector or for neutron interaction which can generate ionizing particles anywhere in the detector volume. A MIPs particle deposits 36 e-h pairs per μm in diamond (Ee/h) [35], therefore passing through a detector of 500 μm, the particle will deposit only $Q_0 = E_{e/h}\, d\, q = 2.9$ fC. These cases are more complex and will be studied in more detail in the following sections.

The performance of a diamond detector is graded by the charge collection efficiency (CCE) or by the charge collection distance (CCD). The CCE is defined as the total measured charge over the total generated charge (4.9), while the CCD is the average distance charge carriers travel before being trapped (4.10). The CCD can also be defined in terms of electron mobility (μ) and lifetime (τ) [35].

$$CCE = \frac{Q_m}{Q_0} \tag{4.9}$$

$$CCD = \frac{Q_m}{Q_0} d \tag{4.10}$$

$$CCD = (\mu_e \tau_e + \mu_h \tau_h) E \tag{4.11}$$

These quantities give an insight to the quality of the diamond detector because charge carriers that get trapped while drifting towards the electrodes stop contributing to the total measured induced charge. Under ideal conditions, all charge generated by an impinging ion is measured as it drifts towards the electrodes. However, charge carriers can be trapped and/or recombined before reaching the electrode resulting in a decrease in the CCE [31]. Unirradiated scCVD based diamond detectors typically have 100 % CCE while pCVD detectors only achieve between 40 % to 60 % CCE. This is mainly due to charge loses at the grain boundaries [36].

3.1. Effects of defects in diamond on charge transport

Any distortion to the periodicity of the diamond lattice or different impurities, influence the electronic and phononic transport properties of the material and possibly creates traps for the

generated charge carriers. The charge carrier lifetime is inversely proportional to the trap density (n_{trap}), carrier thermal velocity (v_{th}) and trapping cross-sections (σ).

$$\tau = \frac{1}{\sigma v_{th} n_{trap}}$$

The energy levels of these traps can be located in the bandgap, stopping the charge carriers from drifting towards the detector electrodes. Once trapped, the charge carriers can be detrapped or recombine leading to a lower detector CCE [37]. Charge carriers can be promoted back to the conduction band by phonons, however this detrapping time is exponentially proportional to the lattice temperature. It ranges from ps at room temperature and increases to μs at cryogenic temperatures [30].

At cryogenic temperatures, the dominant mechanism of charge carrier trapping is hypothesized to be due to the creation of excitons. Excitons were first proposed by Y. Frenkel in 1931 and have since been observed in silicon and in diamond [38]. When an electron is promoted to the conduction band leaving behind a hole, due to the Coulomb force the electron can be bounded to the hole in a hydrogenic state, this state is referred to as an exciton. The binding energy of this bond is 80.0 ± 0.5 meV [39]. The exciton lifetime at room temperature is very short due to the energy in the diamond lattice being high enough to break the exciton bond and promote the electron to the conduction band. However, at cryogenic temperatures, this is not the case and the exciton lifetime increases significantly. The increased lifetime of the exciton also increases the probability that the exciton will recombine (the electron and hole with recombine). This recombination leads to less charge carriers drifting in the detector and therefore less current induced on the electrodes. The lifetime of an exciton is the combination of two processes, $\frac{1}{\tau} = \frac{1}{\tau_{rec}} + \frac{1}{\tau_{evap}}$, which are temperature depended. Table 3.3 summarizes the exciton lifetime with temperature [30].

Table 3.3 - Exciton Lifetime dependence on temperature [30]

T [K]	**τ_{evap}**	**τ_{rec}**
300	30 ps	< 10 ns
100	10 ns	10 ns
50	150 μs	

However, in the presence of a large electric field, the electron and hole pair should start drifting as soon as they are created, decreasing the probability of entering into an exciton state. It is theorized by Jansen [30], [40] that this is not observed due to a not even distribution of the electric field in the volume of generated e-h pairs.

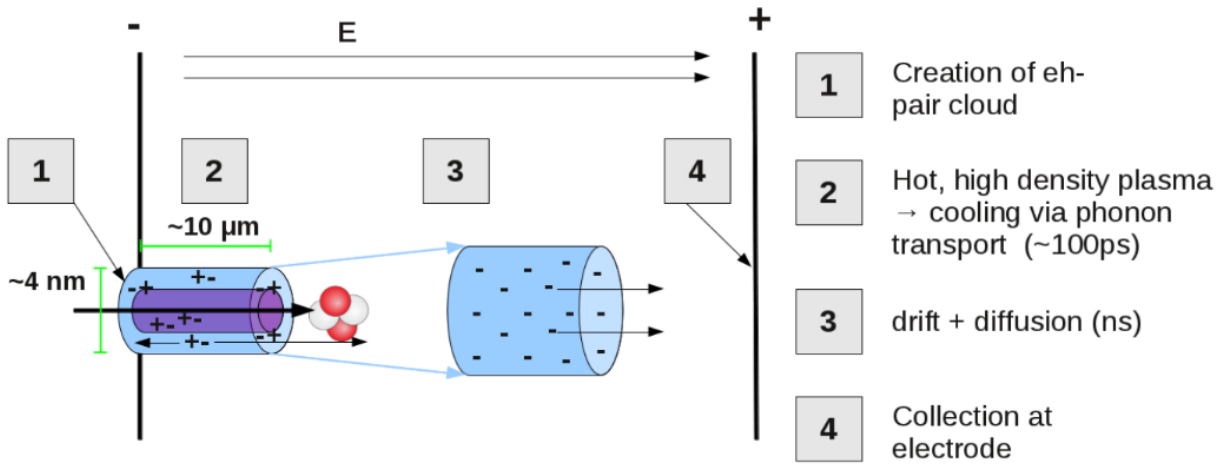

Figure 3.2 - e-h pair screening effect [41]

As illustrated in Figure 3.2, as a particle impacts the diamond detector (an alpha particle is illustrated), it creates a plasma cloud of e-h pairs along its trajectory. The dimensions of this plasma cloud depends on the type and energy of the ion. Due to the density of this plasma cloud, e-h pairs located inside the plasma cloud are influenced less by the external electric field effectively decreasing the rate of separation of the charge carriers. This screening effect increases the probability of exciton formation inside the plasma cloud leading to recombination and only the e-h pairs located on the outside of the plasma cloud contribute to the induced current of the detector electrodes [30]. This implies that the amount of charge carriers collected in the inner region of the plasma cloud depends on the strength of the electric field. Therefore, if a higher bias voltage is applied across the detector, the CCE should increase at cryogenic temperatures. Furthermore, impinging radiation which creates a plasma cloud of lower density will be less affected by this phenomenon.

3.2. Polarization phenomenon in scCVD diamond

Not all charge carriers trapped in defects recombine instantly but accumulate in defect sites along their drift path in the diamond bulk. This leads to a phenomenon known as polarization which can significantly decrease the CCE of the detector. Holes drift toward the negative electrode, resulting in a higher density of holes being trapped closer to the negative electrode. While electrons drift towards the positive electrode, resulting in a higher density of trapped electrons closer to the positive electrode. The separated trapped charge creates an internal electric field which acts in the opposite direction to the external electric field created by applying a bias potential at one of the detector electrodes, effectively decreasing the electric field strength in the detector. This is visually depicted on the right hand side of Figure 3.3 [42].

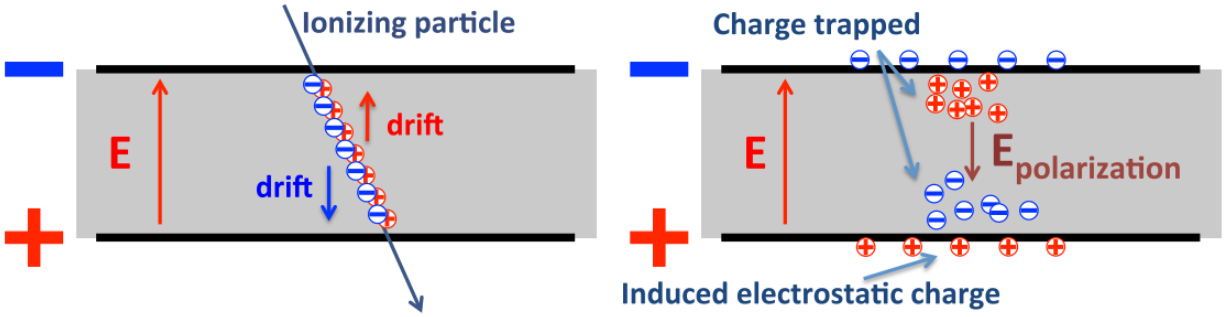

Figure 3.3 - Polarization [42]

The decreased electric field strength increases the probability of recombination and deteriorates charge transport properties resulting in lower charge collection. The degree of polarization is not constant but increases with more accumulated charge causing drastic differences in experiments depending on the fluence of radiation. Furthermore, the built up space charge can be randomly detrapped causing a sudden burst of charge carriers at random periods [31]. Polarization is not only affected by the space charge in the bulk of the detector but is also affected by the type of contact between the detector electrode and diamond. A Schottky contact can enhance the trapping of charge carriers leading to more polarization. [43].

For experiments to be accurate and reproducible, steps must be taken to mitigate the effects of polarization. As polarization cannot be completely avoided, it can be minimized or reversed during an experiment by applying one of the following techniques [30], [42], [44]:

- **Limiting the particle flux on the detector:** Decreasing the number of e-h pairs generated will decrease the amount of space charge trapped in the detector, minimizing polarization.
- **Increasing the bias (external field strength):** Decreases the probability of charge trapping and more space charge has to accumulate to polarize the detector to the same degree.
- **Alternating the bias (changing the bias polarity):** Switching the polarity of the external electric field will cause the trapped space charge to move in the opposite direction and recombine effectively depolarizing the detector.
- **Detrapping charge carriers using light:** Diamond is a wide bandgap semiconductor and not sensitive to visible light. However, light will have enough energy to promote trapped charges into the conduction band from trap levels inside the bandgap.

3.3. Low temperature dependents

Unlike with silicon detectors, lowering the temperature of a diamond detector does not decrease the noise level significantly. Diamond is a wide bandgap semiconductor and at room temperature, the lattice does not have enough energy to promote electrons across the bandgap. However, as with silicon detectors, the mobility of charge carriers does increase due to lower lattice vibrations as the temperature is decreased. The mobility along with the drift velocity saturates to a maximum value below 100 K [30], [40], [45]. Furthermore, negative differential mobility (NDM) was also observed in diamond below 140 K. Negative differential mobility occurs when the electron mobility decreases with increasing electric field strength. NDM can lead to Gunn oscillations, introducing a high frequency oscillation to the output current of the detector. This was only observed at low electric field strengths under 0.2 V/μm [46].

Literature on diamond detector behavior at temperatures under 80 K is very scarce. As mentioned earlier, only a few research papers were found for the study of radiation hardness and charge transport at cryogenic temperatures. The most relevant work is by Jansen [30] who investigates the charge mobility in diamond from room temperature to 2 K and discovered a significant drop is detector efficiency which was attributed to exciton recombination. The results of this work are summarized in Figure 3.4. Figure 3.4 illustrates the measured charge for a 5.5 MeV alpha particle hitting a diamond detector in the temperature range 2 K < T < 300 K for electrons and holes. In both figures, at 300 K, full deposited charge is measured, the CCE is 100 %. However, as the temperature decreases the amount of charge measured starts to decrease sharply around 150

K before reaching another lower plateau around 60 K. The measured charge decreases with temperature while the deposited charge is constant.

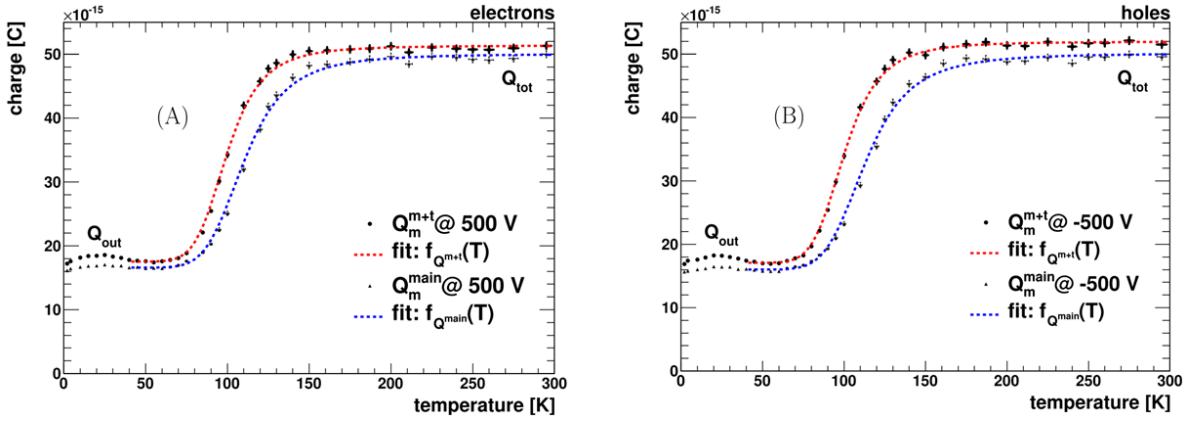

Figure 3.4 - Measured charge as a function of temperature [30]

More recently, diffusion and lifetimes of excitons in diamond at cryogenic temperatures were investigated in more detail with the motivation of developing deep ultraviolet emitting diodes. The large binding energy of excitons in diamond leads to light emission at 235 nm at room temperature which is effective for use in sterilization but still safe for human exposure [47]. Since it is postulated that the main reason so the decrease in CCE of a diamond radiation detector at cryogenic temperatures is due to the formation and recombination of excitons, the results of work in this field is also explored. It is observed that the density of excitons in a charge cloud of free carriers varies with the total carrier density and temperature. This relationship can be modeled using the mass-action law, which is also referred to as the Saha equation:

$$\frac{n_{eh}^2}{n_{ex}} = AT^{\frac{3}{2}} e^{\left(\frac{-E_{ex}}{k_B T}\right)} \tag{4.12}$$

the ration of free carrier density (n_{eh}) to the exciton density (n_{ex}) is a factor of temperature (T), exciton binding energy (E_{ex} = 80 meV), Boltzmann constant (k_B) and a coefficient A which represents the exciton density of states and was experimentally estimated to be $4.4 \pm 2.7 \times 10^{14}$ $cm^{-3}K^{-3/2}$ [48]. From equation 4.12, it can be concluded that the density of excitons is significantly higher at cryogenic temperatures.

3.4. μ-loss Detector for DONES

Preliminary research on the feasibility of using diamond detectors for μ-loss monitors to measure the neutron flux for the Linear IFMIF Prototype Accelerator (LIPAc) has been performed by a group from CEA Saclay Nulcear Research Center. This section will summarize their publish work presented in [3]–[5], [49] since the DONES facility is an evolution of LIPAc and illustrated in Figure 3.5.

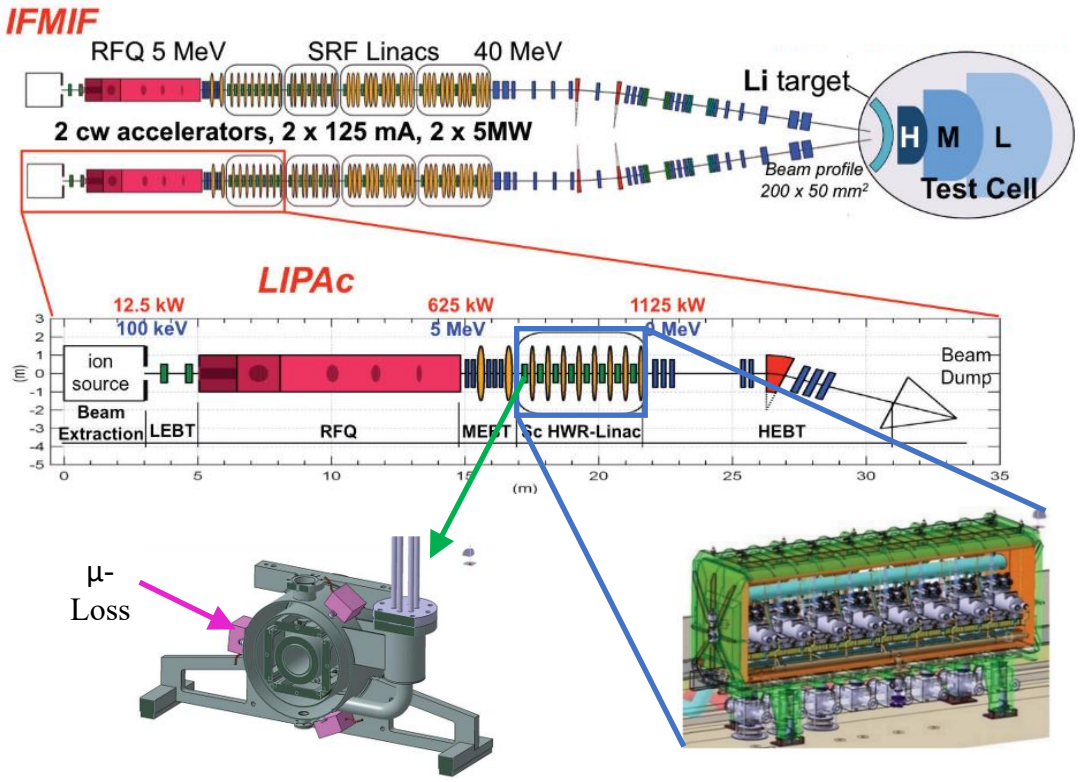

Figure 3.5 - μ-loss monitor location

The largest beam halos are expected right before the superconducting solenoid focusing magnets located inside the half wave resonator (HWR) cryostat and it is therefore recommended that the μ-loss monitors be placed as close as possible to the beam axis right next to the magnets as illustrated in Figure 3.5. Furthermore, to provide redundancy and angular information, three μ-loss monitors will be placed at 120° to each other around the beam pipe. Radiation at this location will be caused by the emission of secondary particles from the interaction of the deuterium beam with the beam tube wall. Neutron are generated from deuterium breakup, D-D reactions, along with

γ-rays and x-rays from the superconductive cavities. The neutron and γ flux at the μ-loss detector location was simulated for the first HWR module which accelerates the deuterium beam from 5 MeV to 9 MeV. The simulated energy spectra are displayed in Figure 3.6 where the top plot (a) contains both the neutron and γ spectrum on a logarithmic energy (x-axis) scale, while plots (b) show the same spectrum separately. It can be concluded from these spectrums that the μ-loss monitors should be sensitive to neutrons up to a few MeV in energy and able to discriminate these neutrons in a γ background with energies up to 10 MeV. X-ray radiation is also expected to be significant inside the HWR cryostat, however this has not yet been simulated.

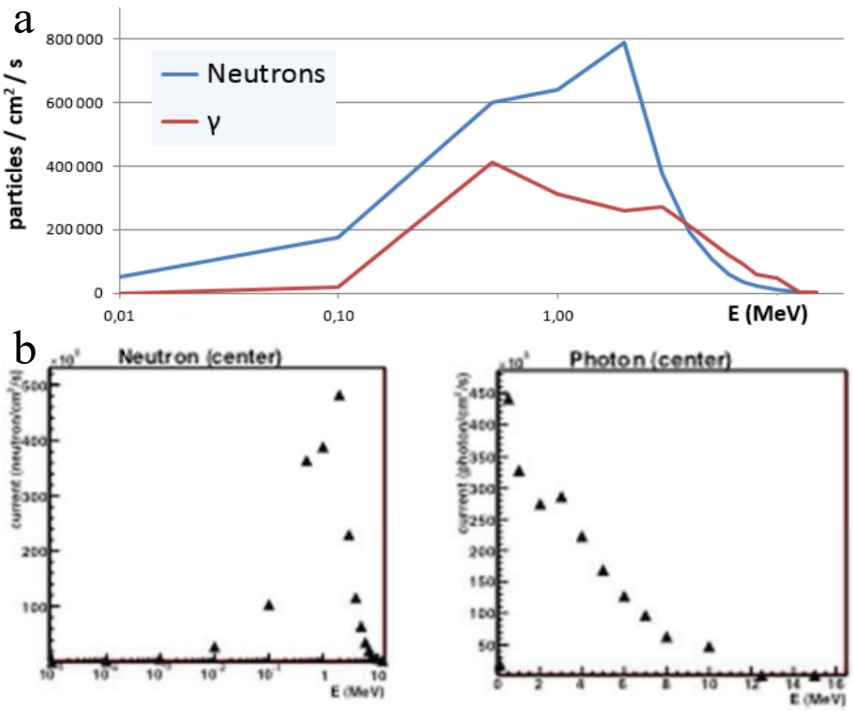

Figure 3.6 - Radiation at μ-loss monitor location. a) combined plot, logarithmic energy scale. b) separate plots, linear energy scale for γ radiation

A few experiments were performed by the group to confirm the operation of a diamond as a μ-loss monitor. Jan Egberts [3], as part of his PhD thesis, tested a diamond detector in a Dewar with a Californium (^{252}Cf) source at 77 K using liquid nitrogen and at 4.2 K using liquid helium. ^{252}Cf decays to Curium (^{248}Cm) by emitting a 6.1 MeV α particle with 97% probability. More importantly, ^{252}Cf has a 3% probability of undergoing spontaneous fission producing on average 3.75 neutrons with a most probable energy of 0.7 MeV and average energy od 2.1 MeV [50]. Since the source was placed outside of the Dewar, only the neutron spectrum was expected on the

diamond. However, γ of energies below 150 keV are also emitted through the two decay chains of ^{252}Cf. The resulting shape of the energy spectra acquired at lower temperatures matched the room temperature spectrum. The only difference was in the spectra high which was expected due to the lower charge collection efficiency of diamond at lower temperatures. This confirmed that the diamond detector works at cryogenic temperatures. However, they did not confirm that the detector registered neutrons because no differences in the energy spectra was observed when a CH_2 neutron absorber was placed between the ^{252}Cf source and the diamond. Experiments with neutrons were performed only at room temperatures using a particle accelerator. Neutrons of 0.6, 0.75, 1.2 and 2.1 MeV were generated using various beam-target combinations. The resulting neutron energy loss spectra discriminated based on time-of-flight with an associated γ emission are presented in Figure 3.7.

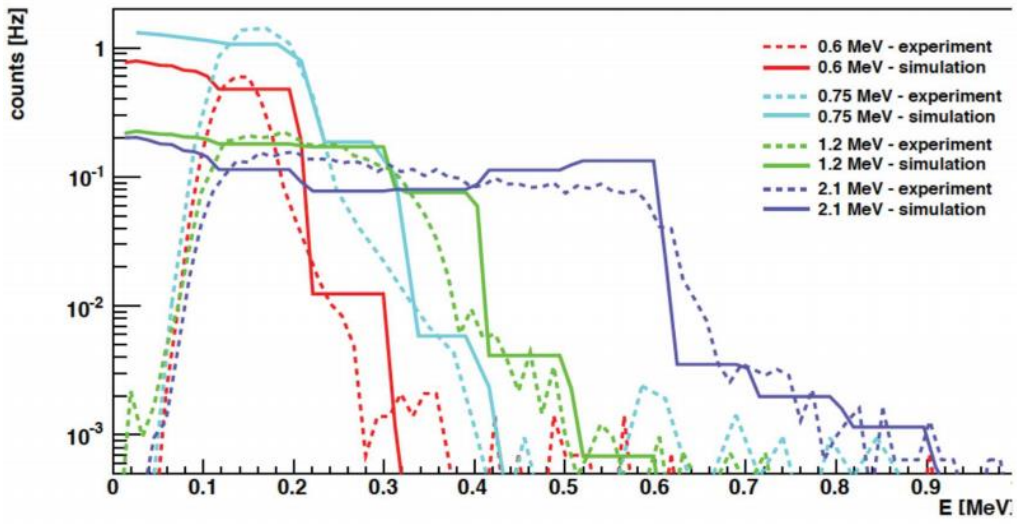

Figure 3.7 - Neutron energy loss spectra and simulations

Furthermore, experiments were also conducted to test the Front-End Electronics (FEE) to estimate the effects of the superconducting solenoid, cable length and preamplifier placement will have on the acquired signal from the detector. Due to the μ-loss monitor position inside the HWR cryomodule, a minimum cable length of 3 meters will separate the diamond from the preamplifier. Due to the low capacitance of diamond, the length and therefore capacitance of the cable itself will greatly impact the final noise in the signal at the data acquisition system. It is therefore proposed to place a broadband radiation hard amplifier next to the cryostat three meters from the detector followed by another 20 meter cable leading to the electronics room as illustrated in Figure 3.8. The

board band amplifier was used with a threshold counter/scaler to determine the rate of particles impinging on the diamond detector. The experiment was performed using a Cobalt-60 (^{60}Co) γ source and the signal arriving at the counter had a sufficient signal to noise ratio for discrimination based on threshold. Further experiments were proposed to use a second shaping amplifier in the electronics area with an analog to digital converter (ADC) to obtain the full energy deposition spectrum. However, no publications were found for this proposal.

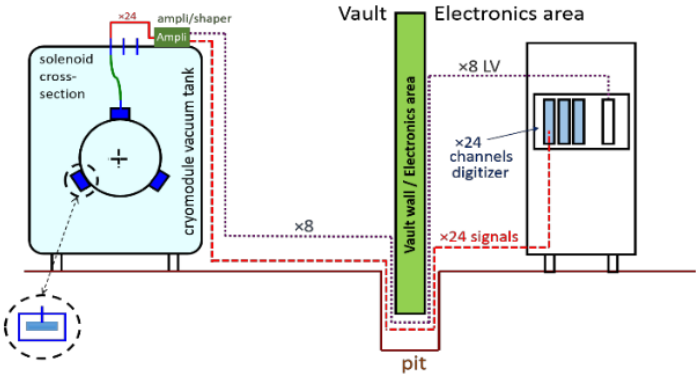

Figure 3.8 - Front End Electronics Setup

Additional experiments were performed by the RD40 group at CERN at low temperatures but only to evaluate the radiation hardness of diamond detectors when exposed to large levels of radiations from proton beams at the Large Hadron Collider (LHC). All performed experiments confirm that a diamond detector can function as a μ-loss detector. However, many other aspects of must be explored to successfully create a μ-loss detector. This work will outline these aspects and provide an overview of these fields.

Experimental Setup at the Ruđer Bošković Institute

In order to add to this pool of knowledge, we are currently developing a diamond based detectors that can operate at cryogenic temperatures. We utilized a scCVD diamond produced by Element Six Ltd. with and area of 4.7 x 4.7 mm^2 and 300 μm thickness. The top and bottom of the crystal was metalized in the Diamond Sensors Laboratory of CEA-LIST with 200 nm thick tungsten in a coplanar geometry with an area of 3 x 3 mm^2. The diamond was mounted on an aluminum nitrate ceramic PCB and bonded to 70 μm copper electroless nickel immersion gold

(ENIG) coated leads with silver paste. In order to monitor the temperature of the diamond accurately required a cryogenic sensor to be placed in close proximity. A Cernox CX-1070 temperature sensors was also mounted using silver paste to have the same thermal connection with the PCB as the diamond. The detector assembly was mounted on the cold-head of a Leybold-Heraeus RPK400 cryopump along with a 25 Ohm resistor for temperature regulation. The whole setup was positioned in a small chamber mounted downstream of the ion microprobe chamber, with the detector being aligned with the axis of the microbeam.

Using this setup, a stable operating temperature of 47 K was achieved and measured using a Lake Shore Cryogenics Model 211 Temperature monitor. The heating element and the temperature sensor were connected to feedthroughs on the chamber using a phosphor bronze (CuSnP alloy) single lead wire which is optimized for cryogenic applications. The detector was connected with a shielded cable which limited the lowest achievable temperature by the system due to thermal leaks. A diamond charge amplifier CSA1 from CIVIDEC which incorporates a preamplifier and a shaping amplifier in one package was mounted to the outside of the chamber and used for biasing the detector and signal acquisition. The analog output of the detector was digitized using a 250 MSPS 14 bit ADC and further processed by an Field Programmable Gate Array (FPGA) [51]. The FPGA was reprogrammed to read the temperature values from the temperature monitor and synchronize the measurements with PHA of the signals from the detector.

This setup allowed us to reproduce the results of other researchers, presented in this work, which showed a decrease in the diamond detector CCE with temperature when irradiated with alpha particles. Furthermore, this work has been expanded to include irradiation with hydrogen, lithium, and carbon ions where a similar decrease in CCE was observed for all ions. However, the decrease in CCE was not the same for all ions. Most notably, the CCE decreased the least for hydrogen giving further insight into the mechanism behind this phenomenon. From this study, it was also concluded that by increasing the bias on the detector, the CCE at low temperatures recovered slightly [52].

A new experimental setup must be created to allow for measurement with higher bias voltages and the signal processing chain must be upgraded to improve the system response to noise. The largest contributors of noise have been identified to be due to the relatively large distance from the detector to the preamplifier, microphonic noise from the vibrations of the cryopump and interference from the axillary equipment required to operate the accelerator. Some of these sources of noise can be

minimized through setup changes while others can be filtered out digitally in the FPGA. The frequency spectrums of signals both from a charge sensitive and current sensitive preamplifier setup must studied in order to develop optimized digital filters which can be implemented in a FPGA. The filters must be designed in such a way to remove noise while keeping the signal shape to allow for subsequent neutron-gamma discrimination. Due to the fast response times of diamond detectors, the feasibility of utilizing charge sensitive preamplifiers for pulse shape analysis at cryogenic temperatures must be investigates. Following this investigation, discrimination algorithms to filter neutrons from the gamma background must be programmed into the FPGA firmware and adopted for signals at cryogenic temperatures. Some of the discrimination techniques mentioned in this work may work at cryogenic temperatures and this must be investigated further.

4. DETECTOR SIGNAL PROCESSING

As described above, the signal level at the output of a diamond detector is very small and amplification is required to limit the influence of noise and allow for processing to extract information. This is achieved by placing a preamplifier as close as possible to the detector. There are three types of preamplifiers used with radiation detectors: voltage sensitive, current sensitive and charge sensitive amplifiers. For the scope of this work, the focus will be on the latter two.

4.1. Preamplifiers for radiation detectors

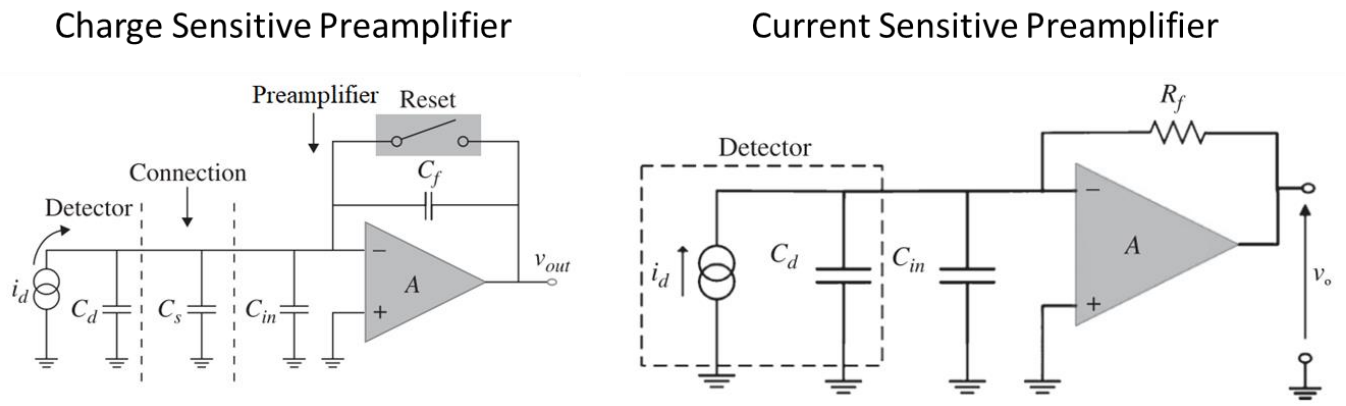

Figure 4.1 - Charge Sensitive and Current Sensitive Preamplifier schematic [53]

The voltage at the output of the charge sensitive preamplifier is obtained by:

$$v_{out} = -\frac{Q_0}{\frac{A+1}{A}C_f + \frac{C}{A}} \tag{5.1}$$

where $C = C_d + C_{in} + C_s$, that is the sum of the detector, cable, and preamplifier capacitance. Most preamplifiers have a large open loop gain ($A >> 1$), and the output voltage can be approximated to:

$$v_{out} \approx -\frac{Q_0}{C_f} \tag{5.2}$$

therefore, the output voltage is determined by the feedback capacitor. In practice, not all charge induced in the detector is transferred to the feedback capacitor, some is lost to other input capacitances. The ratio of the charge transferred to the preamplifier can be expressed as:

$$\frac{Q_f}{Q_0} = \frac{Q_f}{Q_{loss} + Q_f} = \frac{1}{1 + \frac{C}{(A+1)C_f}} \tag{5.3}$$

Decreasing the sum of input capacitances (C) results in more induced charge to be transferred to the feedback capacitor. Therefore, it is better to use detectors with low capacitance and minimize the cable length between the detector and the preamplifier. Charge sensitive preamplifiers are characterized by a parameter called sensitivity which is expressed in units of mV/MeV. Combining equations 4.7 and 5.2, yields the sensitivity parameter:

$$\frac{v_{out}}{E} = \frac{q}{E_{pair} C_f} \tag{5.4}$$

In the charge sensitive preamplifier schematic on the left of Figure 4.1 a reset switch is shown which is required to discharge the feedback capacitor, otherwise the output voltage would saturate. There are many reset strategies employed in preamplifiers, however the most common one is the introduction of a large resister parallel to the feedback capacitor which allows for continuous discharging.

There are two main ways of connecting the detector to the preamplifier and the high voltage supply: AC coupling through a capacitor or DC coupling without the capacitor as illustrated in Figure 4.2.

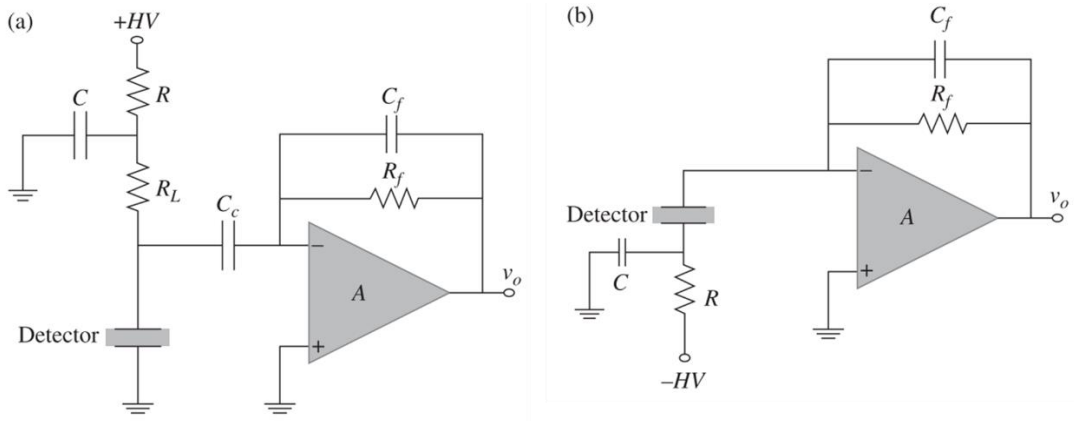

Figure 4.2 - Detector Coupling [53]

The coupling capacitor (C_c) blocks leakage current from the detector from entering the preamplifier which lowers the noise. However, additional noise is introduced by the load resistor (R_L) after the high voltage input filter which is chosen to be as large as possible to limit the voltage drop due to the detector leakage current. DC coupling is beneficial for detectors that have a very low leakage current (below 10^{-14} A) because it eliminated the noise associated with the load resistor and minimizes the stray capacitance which can improve the signal to noise ratio [53].

On the other hand, a current sensitive preamplifier, illustrated on the right side of Figure 4.1, does not have a feedback capacitor and the output voltage is related to the input current by $v_{out}(t) = -i_{in}(t)R_f$ which allows for the shape of the induced current to be directly transferred to a voltage pulse at the output of the amplifier.

4.2. Characteristics of noise

Since the signal induced on the electrodes of a diamond detector is very small, any noise introduced into the system will greatly degrade the accuracy of the information extracted from the signal and impose higher requirements on further pulse processing. The most common types of noise found in a radiation detector system are:

- **Thermal (Johnson) Noise** – White noise caused by the random motion of free charge carriers in a resistive material. Increases with system bandwidth without limits.
- **Shot Noise** – White noise caused by charge carriers having a discreate amount of charge. This introduces random fluctuation of current around an average value. The leakage current is one source of this type of noise.

- **Flicker Noise (1/f noise)** – Frequency dependent noise resulting from the generation and recombination of charge carriers in a semiconductor due to impurities. This type of noise is also generated from the fluctuation in conductivity due to imperfect contact between two materials. The input transistor of the preamplifier generates 1/f noise.
- **Dielectric noise** – Frequency dependent noise which increases with frequency. Any fluctuation in the dielectric properties of a material caused by temperature, mechanical vibration, or age will introduce noise. This can be reduced by using dielectric materials with low losses, such as quartz, ceramics, Teflon, and polystyrene.

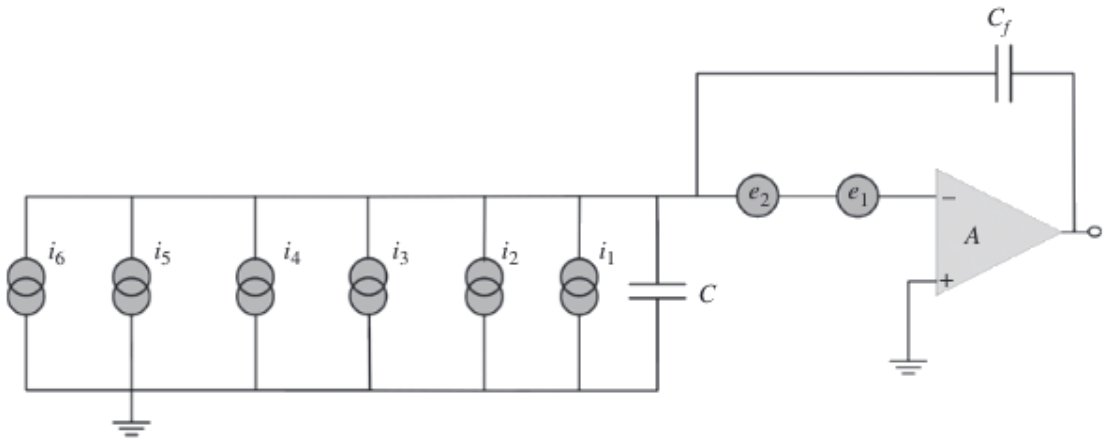

Figure 4.3 - Noise equivalent circuit of a AC coupled charge sensitive preamplifier

Using the types of noise described above, an equivalent circuit of a AC couple preamplifier can be constructed as illustrated in Figure 4.3 where each component is replaced by a noise source connected in series or parallel. The two serial voltage noise sources (e_1 and e_2) represent the input transistor thermal and 1/f noise for which the voltage noise density can be written as:

$$\frac{de_1^2}{df} = 4kTR = 4kT\frac{\gamma}{g_m} = 4kT\frac{0.7}{g_m} \tag{5.5}$$

$$\frac{de_2^2}{df} = \frac{A_f}{f} \tag{5.6}$$

where γ depends on the channel length of the FET and is usually 0.7 while A_f is a characteristic constant for the transistor. The parallel noise sources are summarized in Table 4.1.

	Description	Expression
i_1	Shot noise of the transistor gate leakage current	$\frac{di_1^2}{df} = 2qI_g$ (5.7)
i_2	Feedback resistor thermal noise	$\frac{di_2^2}{df} = \frac{4kT}{R_f}$ (5.8)
i_3	Bias resistor thermal noise	$\frac{di_3^2}{df} = \frac{4kT}{R_b}$ (5.9)
i_4	Induced transistor gate current noise	$\frac{di_4^2}{df} = S_{ws}\omega^2 C_{gs}^2 \delta$ (5.10)
i_5	Shot noise from the detector leakage current	$\frac{di_5^2}{df} = 2qI_L$ (5.11)
i_6	Dielectric noise	$\frac{di_6^2}{df} = 4kT(DC_D)\omega$ (5.12)

Table 4.1 - Parallel noise sources

The total noise power density can be calculated by evaluating the above circuit with the presented noise sources, yielding the following expression:

$$\frac{dv_o^2}{df} = \left[4kT\frac{0.7}{g_m} + \frac{A_f}{f}\right]\frac{\left(C + C_f\right)^2}{C_f^2} + \left[2q\left(I_L + I_g\right) + 4kT\left(\frac{1}{R_f} + \frac{1}{R_b}\right)\right]\frac{1}{\omega^2 C_f^2} + \frac{4kT(DC_D)}{\omega C_f^2} \quad (5.13)$$

The above equation can be rewritten as:

$$\frac{dv_o^2}{df} = \frac{1}{C_f^2}\left[aC_{tot}^2 + \left(A_f C_{tot}^2 + \frac{b_f}{2\pi}\right)\frac{1}{f} + \frac{b}{(2\pi)^2}\frac{1}{f^2}\right] \quad (5.14)$$

where the constant a is the series white noise, b is the dialectic noise and b_f the parallel white noise. A similar approach can be applied to a current sensitive preamplifier to derive an expression of the noise power density. The main difference between the two preamplifiers is the size of the feedback

resistor and the presence of the feedback capacitor. Since the value of the feedback resistor has to be smaller for the current sensitive preamplifier, the level of noise is going to be higher due to the thermal noise [53].

Noise is also introduced into the system through interference (parasitic noise), the most common types being electromagnetic interference (EMI), ground related interference and vibrations. EMI is the result of stray magnetic fields from surrounding equipment, such as power supplies, vacuum pumps, pressure gauges and computers. All electronic devices emit electromagnetic waves which can be picked up by the sensitive electronics at the input of the preamplifier. EMI falls off with the $\frac{1}{d^2}$ rule and therefore moving sources of EMI further way from the detector is the best solution. However, this is not always possible and therefore it is good practice to enclose the detector in a Faraday cage. It is also important to ground the faraday cage because parasitic capacitance between the circuit and shield can provide a feedback path from the output to the input. Furthermore, ground related interference result from ground loops. Ground loops are created when the ground connection between instruments is not at an equipotential resulting in a current to flow between the grounds of difference instruments. Noise is also added to the system by vibration (Microphonic Noise), mechanical vibrations of the detector and preamplifier cause slight changes in the capacitance throughout the system leading to noise. This noise is usually observed in signals at multiples of the vibration frequency and therefore can be filtered out.

The noise added by the preamplifier and amplifier is expressed as equivalent noise charge (ENC). ENC is defined as the amount of charge required to be added to the input of a preamplifier that would change the output voltage by only the root mean square (RMS) value of noise. In other words, the amount of charge that yields a signal to noise ratio of one [54]. The signal to noise ratio is defined as the ratio of the mean pulse height to the RMS value of the noise.

$$\frac{ENC}{Q} = \frac{V_{noise}}{V_{pulse}} = \frac{E_{fwhm}}{2.35\, E_{pair}} \tag{5.15}$$

4.3. Digital signal processing of preamplifier signals

As described in the previous section, a charge sensitive amplifier integrates the current pulse induced on the electrode of the detector and therefore the amplitude of the pulse at the output of the preamplifier is proportional to the energy deposited by radiation in the detector. However, noise is superimposed on the signal and signal processing techniques must be applied to improve the signal to noise ratio and increase the accuracy of the pulse height analysis (PHA).

Signal processing increases the signal to noise ratio by attenuating components of the input signal that lie outside the frequency range of the signal of interest. Due to the nature of the signal produced by the preamplifier, there is always a compromise between noise minimization and signal alteration. Mathematically it is possible to compute the optimal filter by representing output signal from the preamplifier in the form $s(t) = Af(t) + n(t)$, where A is the amplitude of the signal, f(t) is the waveform of the pulse and n(t) is the noise in the signal. The output of the filter can be calculated convoluting the input signal with the impulse response function of the filter. Taking the Fourier transform of the input and filter impulse response ($h(t)$), convolution becomes multiplication in Fourier space. The output of the filter can then be calculated the taking the inverse Fourier transform as follows:

$$s(t) = Af(t) + n(t) \tag{5.16}$$

$$S(\omega) = AF(\omega) + N(\omega) \tag{5.17}$$

$$v_o(t) = \frac{A}{2\pi} \int H(j\omega)F(\omega)e^{j\omega t}d\omega \tag{5.18}$$

Similarly, the RMS noise at the output of the filter can be calculated with the noise power density of the filter $N(\omega)$:

$$v_n^2 = \frac{1}{2\pi} \int |H(j\omega)|^2 N(\omega)d\omega \tag{5.19}$$

Therefore, the signal to noise ratio (η) is given by:

$$\eta = \frac{A^2}{2\pi} \frac{\left(\int H(j\omega)F(\omega)e^{j\omega T}d\omega\right)^2}{\int |H(j\omega)|^2 N(\omega)d\omega} \tag{5.20}$$

The optimal filter can be calculated by maximizing the above equation. The details procedure for obtaining the solution for the optimal filter from the above relation can be found in literature and will not be outlined here [53]–[55]. The optimum filter for a exponentially decreasing function (as illustrated in the top graph of Figure 4.4) is characterized for the measurement time T by the following function:

$$h(t) = f(T - t) \tag{5.21}$$

which is the time inverted input signal delayed by the measurement time. The output of such a filter is:

$$v_o(t) = e^{-\frac{|t-T|}{\tau_c}} \tag{5.22}$$

where τ_C is the corner time constant representing the inverse frequency at which the contribution of the serial (a) and parallel (b) noise are equal, $\tau_c = C\sqrt{\frac{a}{b}}$, while C is the total input parallel capacitance (C_d + C_i). The optimum filter has a cusp shape with infinite length. The input and output of the optimum filter are illustrated in Figure 4.4.

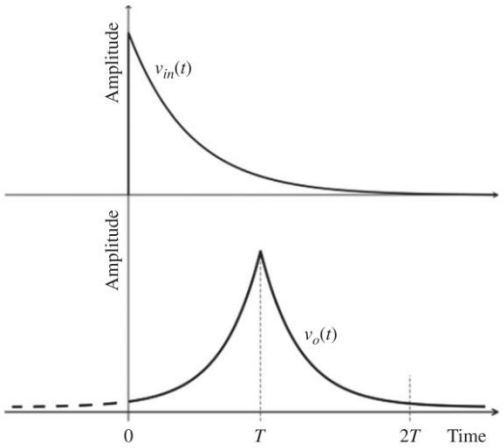

Figure 4.4 – The top graph shows the exponentially decaying signal from a preamplifier while the bottom graph shows the output of an optimum filter. [53]

The cusp filter described above is the theoretical optimal filter for radiation detector systems, however it is not practical and cannot be implemented. The sharp rise to maximum amplitude makes amplitude measurement difficult and makes it prone to ballistic effects. Furthermore, the slow signal return to baseline is prone to pile up effects due to the stochastic nature of radiation which further deteriorate the effectiveness of the filter with higher event frequencies. Since the cusp filter is the optimum filter in terms of signal to noise, it is useful as a comparison to other filters which are more practical to implement. In this work we will consider only two practical filter types and their performance compared to the optimum infinite cusp filter are presented in Table 4.2 [14].

Table 4.2 - Comparison of filter performance to the optimum filter

Filter	S/N ratio to optimum filter
Infinite Cusp	1
Triangular	0.930
CR-RC	0.736

As mentioned above, the signal to noise ratio is improved by limiting the frequency response of the system, effectively creating a bandpass filter which attenuates frequencies that are below and above the signal frequency. The most commonly used practical filter for pulse processing is the CR-RC filter, consisting of a highpass filter in series with a lowpass filter as illustrated in Figure

4.5. The highpass section is labeled the differentiator and the lowpass section, the integrator since they integrate and differentiate the input pulse, respectively.

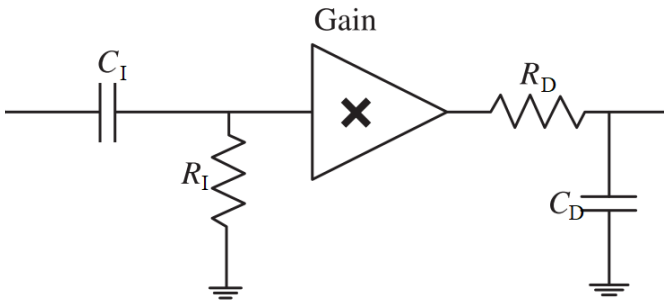

Figure 4.5 - CR-RC Filter

Due to its simplicity, it is easy to implement and easy to analyze. The transfer function for each part of the filter can be easily derived to be:

$$H_I(s) = \frac{s\tau_I}{1 + s\tau_I}\ , \tau_I = R_I C_I \tag{5.23}$$

$$H_D(s) = \frac{1}{1 + s\tau_D}\ , \tau_D = R_D C_D \tag{5.24}$$

$$H(s) = H_I(s) \cdot H_D(s) = \frac{s\tau_I}{(1 + s\tau_I)(1 + s\tau_D)} \tag{5.25}$$

For a unit step input, the output in the time domain is then

$$V_o(t) = \frac{\tau_D}{\tau_D - \tau_I}\left(e^{-\frac{t}{\tau_D}} - e^{-\frac{t}{\tau_I}}\right) \tag{5.26}$$

The best signal to noise ratio for this type of filter is achieved when the integrator and differentiator time constants are equal, $\tau_I = \tau_D = \tau$, therefore the transfer function and output become:

$$H(s) = \frac{s\tau}{(1+s\tau)^2} \tag{5.27}$$

$$V_o(t) = \frac{t}{\tau} e^{-\frac{t}{\tau}} \tag{5.28}$$

The maximum amplitude with such a filter is achieved at t = τ, however the filter introduces a long tail which takes many time constants to return to baselevel. This makes the filter susceptible to pileup events which limit the measurement rate of the system, as will be discussed later.

From Table 4.2, it can be seen that the simple CR-RC filter has a 26 % worse signal to noise ratio than the optimal cusp filter. Better performance can be achieved by a triangular filter which has become the standard filter implemented for radiation detector digital signal processing (DSP). Practically, a trapezoidal filter is used instead of a triangular filter to mitigate ballistic effects which will be discussed later. A trapezoidal filter is essentially a triangular filter where the maximum amplitude is held for a specific time. The transfer function of a trapezoidal filter can be synthesized by examining the input and required output functions. The input is, as discussed above, an exponentially decaying signal with a time constant (τ) and amplitude (E).

$$f_{IN}(t) = Ee^{-\frac{t}{\tau}} \Rightarrow F_{IN}(z) = E\frac{z}{z-\beta} = E\frac{1}{1-\beta z^{-1}}, \beta = e^{-\frac{T}{\tau}} \tag{5.29}$$

β is known as a pole-zero cancellation coefficient which is depended on the sampling period of the digitizer (T). The output function can be synthesized by examining the trapezoidal shape illustrated in Figure 4.6 [56], [57].

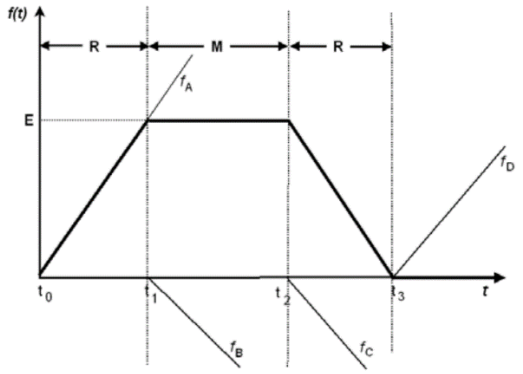

Figure 4.6 - Synthesizing a trapezoidal function

$$f_{OUT}(t) = f_A(t) + f_B(t) + f_C(t) + f_D(t) \tag{5.30}$$

$$F_{OUT}(z) = \frac{E}{R}(1 - z^{-R})\left(1 - z^{-(R+M)}\right)\frac{z^{-1}}{(1 - z^{-1})^2} \tag{5.31}$$

Combining equations 5.29 and 5.31, to get the transfer function of the filter:

$$H_{TRZ}(z) = (1 - z^{-R})\left(1 - z^{-(R+M)}\right)\frac{(1 - \beta z^{-1})}{1 - z^{-1}}\frac{z^{-1}}{1 - z^{-1}}\frac{1}{R} \tag{5.32}$$

where the parameters R and M represent the represent the trapezoid rise/fall and flat top time, respectively. The transfer function presented above is a combination of a Finite impulse response (FIR) and infinite impulse response (IIR) filter which can be implemented is a DSP system.

As mentioned above, in real system, factors such as ballistic deficit, pileup and baseline shifts have to be considered when designing filters. These effects will now be explained in more detail. Ballistic deficit refers to the dependence of the pulse height after processing on the rise time of the input signal. Therefore, fluctuations in the charge carrier collection time in the detector can cause variations in the signal amplitude after signal processing. CR-RC filters are more susceptible to this effect than trapezoidal filters because the max amplitude of the signal is held for a longer time in trapezoidal filters. By increasing the time constant of a CR-RC filter, this effect can be minimized but at the expense of increasing the probability of pileup. Pileup occurs when two pulses are close to each other in time causing their pulses to overlap. The second pulse is then superimposed on top of the first pulse because the first signal has not returned to the baseline value before the second signal arrived, causing an incorrect reading of the second pulse height. The same problem occurs if the baseline, the reference point from which signal amplitudes are measures, is not stable. Fluctuations in the baseline value leads to fluctuations in the measurement of the pulse height which degrades the energy resolution of the system. Baseline fluctuations can occur due to high pulse rates, detector leakage current in dc couple systems, uncorrected pole-zero, or thermal drifts in electronic components.

4.4. Ion beam analysis

The processed signal from the detector can give a lot of information about the material or detector being irradiation based on the experimental configuration and ion beams used. Many ion beam analysis (IBA) techniques have been developed to investigate various aspects of materials. For the purpose of this work, we will focus on two techniques, Ion Beam Induced Charge (IBIC) and the Transit Current Technique (TCT). IBIC spectroscopy is a widespread tool used for the characterization of charge transport in semiconductor materials. It utilizes an ion beam on very low current (< fA) from an accelerator to induce charge carriers along the ion path in a detector volume [58]. The performance of the detector can be evaluated by measuring the amount of induced charge acquired by the detector. For this technique a charge sensitive amplifier is used with pulse processing to extract the pulse height which is proportional to the induced current on the detector electrodes. By collecting the height of each pulse over time, a histogram can be crated representing a spectrum of collected charge by the detector as a function of energy. For a mono energetic beam on a detector with 100 % CCE, the pulse height should be always the same resulting in a single peak in the histogram at the specific beam energy. However due to noise in the signal, the peak will be broadened. The full width and half maximum (FWHM) of this peak represents the noise in the detector and signal processing chain. If the CCE of the detector in not 100 %, the peak will shift to lower energies. Additionally, the ion beam can be scanned over the surface of the detector providing 2D information about the efficiency of the detector. By plotting the histogram peak position (energy) for every beam position, a map can be generated of the detector efficiency as illustrated in Figure 4.7. It can be observed from Figure 4.7 that the detector efficiency is lower at the edges of the electrode. Furthermore, TCT utilizes a current sensitive broadband preamplifier and information about charge transport in the diamond detector can be evaluated by the shape, rise, and fall times of the current pulses [11]. Figure 3.1 illustrates an example of a TCT pulse on an oscilloscope with the significance of each portion of the pulse outlined. This method is useful because it can provide information on which charge carrier was generated, how many charge carriers were generated and where. This information can be used by a digital system to discriminate between different types of radiation, specifically between gamma and neutrons in the context of this work. However due to the use of a broadband preamplifier and no signal processing techniques to increase the signal to noise ratio, noise minimalization is essential for TCT.

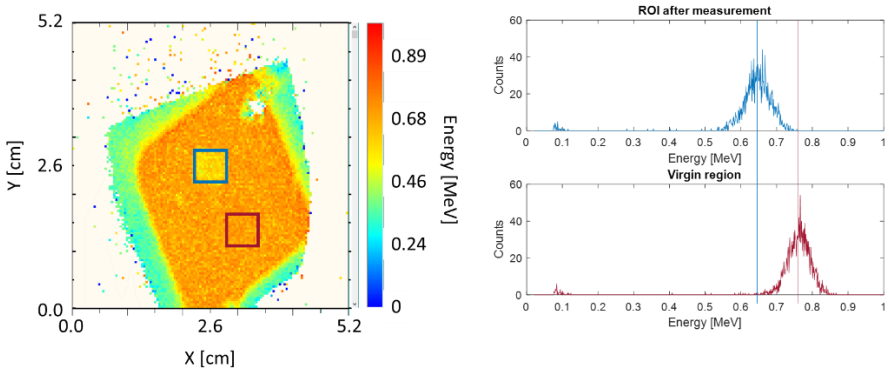

Figure 4.7 - IBIC of a detector

5. NEUTRON DISCRIMINATION

Many techniques have been employed to discriminate neutrons from other forms of radiation both in the digitally and in the analog domain. The main discrimination strategies are either based on detection of associate particles from nuclear reactions (see section 2.2), coincidence measurements or through the analysis of the pulse shape from the detector. Some of these methods have been applied to diamond detectors and they will be investigated here. It should be noted that all these methods have only been demonstrated at room temperature with diamond detectors.

5.1. Neutron spectra obtained with diamond detectors

As mentioned in section 2.2, diamonds are used to detect neutrons indirectly through nuclear reactions which produce ionizing particles. For fast neutrons, the associated reactions are listed in Table 2.1 which produce ionizing particles throughout the detection volume of the diamond detector. These secondary particles create electron hole pairs as they interact with the diamond which drift and induce current in the detector electrodes. The expected spectra are illustrated in Figure 5.1 [59]. The figure on the left shows the spectrum obtained by 20.5 MeV neutrons in black and 8.3 MeV neutrons in blue. Due to the kinematics of the reaction and differences in the amount of energy transferred to the secondary particles, the spectrum shifts with incident neutron energies. The figure on the right of Figure 5.1 shows more spectra for neutron energies from 7.33 MeV to 20.5 MeV. Spectra under 7.33 MeV are not shown since the threshold for nuclear reactions is at 6.2 MeV. Below this threshold, no nuclear reactions take place, and the spectrum is composed only of system noise, gamma, x-ray radiation, and signals generated by neutron recoils with carbon atoms. This creates a “background” spectrum at lower energies whereby analyzing only the height of the signal pulses from the detector, it is impossible to distinguish the source of radiation.

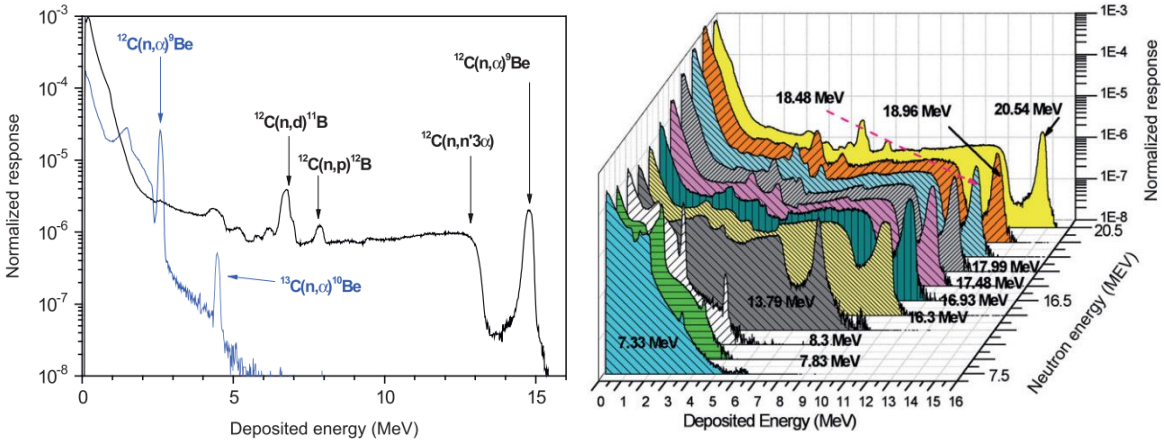

Figure 5.1 - Spectra for Neutrons of 7 to 20 MeV

For energies below the threshold energy for nuclear reactions, only elastic scattering occurs between the neutron and carbon atoms. In this process the carbon atom is recoiled, and this recoil is a movement of charge which also induces current on the detector electrodes. As mentioned in section 2.2, the maximum recoil energy can be calculated, and the spectrum will consist of a continuum of events up to this maximum recoil energy as illustrated in Figure 5.2 [25].

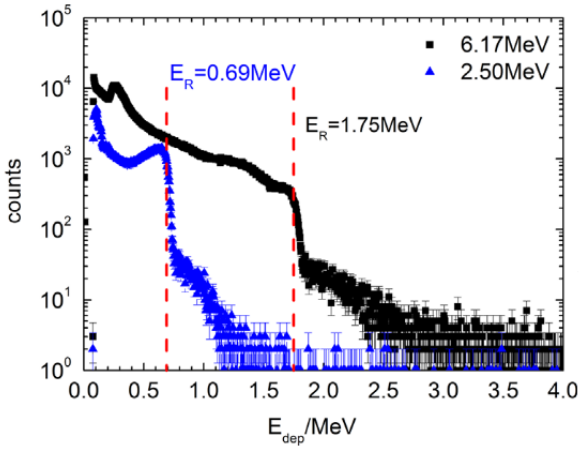

Figure 5.2 - Spectrum of fast neutrons below 6.2 MeV

Neutron flux can be estimated based on the $^{12}C(n,\alpha)^{9}Be$ peak created from the nuclear reaction by neutrons of energies greater than 6.2 MeV. However, as can be observed from the lower energy spectra from Figure 5.1 and Figure 5.2, there is no distinctive peak that can be used to estimate the neutron flux. All features in the spectrum are a superposition of many processes which cannot be

easily isolated. As mentioned in section 2.2, elements that have a higher probability of undergoing nuclear reactions at lower neutron energies can be placed on top of the detector to act as a "converter" layer to transform the neutrons to ionizing particles which can be detected by the diamond detector. Figure 5.3 illustrates spectra obtained by a diamond detector with a ^{6}LiF converter of various thicknesses [17]. The ^{6}Li(n,α)T reaction takes place inside the film and the diamond detects the α and T emitted from the film. This produces two peaks which are distinguishable and can be used to estimate the neutron rate. The figure also shows the impact of converter layer thickness on the spectrum. The thicker the converter layer, the more material which slows down the α and T particles before they reach the diamond detector. This straggling in the converter causes broadening of the peaks in the spectrum. However, the probability of neutron interaction with the converter increases with the thickness leading to a tradeoff between detection efficiency and resolution.

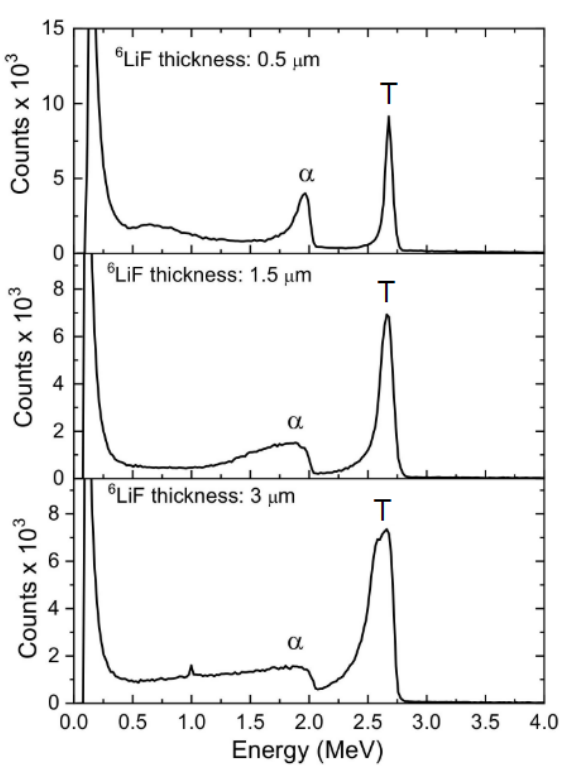

Figure 5.3 - Spectra for neutrons with ^{6}LiF converter layer of various thicknesses

5.2. Discrimination through detector configurations

Discrimination of neutrons can be achieved at the detector by placing a converter layer on top of the detector as was discussed in the previous section. This concept can be taken a step further by sandwiching the converter between two diamond detectors. The single detector configuration is illustrated on the left of Figure 5.4, while the sandwich on the right [60].

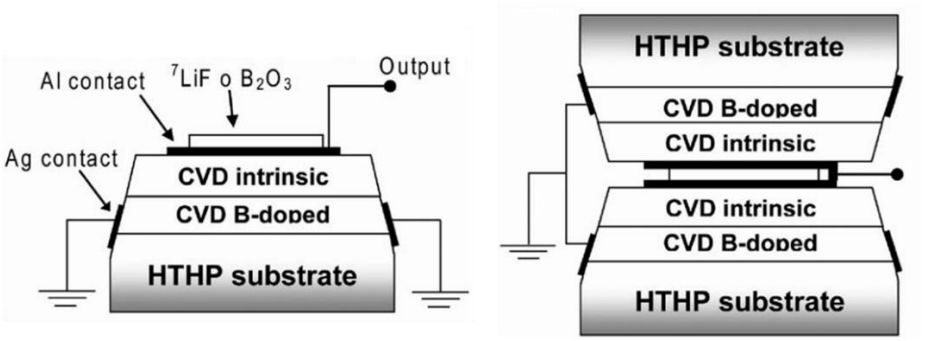

Figure 5.4 - Single and Sandwich Detector Configurations

The single detector (right of Figure 5.4) operates as described in the previous section where the neutron undergoes a nuclear reaction in the converter layer (^{6}LiF or $^{10}B_2O_3$) and the biproducts are detected in the diamond. In the above figure, the intrinsic diamond detector is built upon a boron doped diamond layer for contact purposes and has not been detached from the High Temperature High Pressure (HTHP) substrate from which the CVD diamond was grown, which acts as an insulator. It should also be noted that since the nuclear cross section of the converter layer (see Figure 2.3) drops exponentially for fast neutrons (E > 1 MeV), the detector can simultaneously detector slow and fast neutrons. The sandwich configuration, on the other hand is just a combination of two diamond detectors that share a common convert layer. This configuration increases the detection volume which makes it more efficient at detecting neutrons and allows for all products from the nuclear reaction in the converter layer to be collected (due to energy conservation, the products of the nuclear reaction are emitted at 180° to each other). Furthermore, if the two detectors in the sandwich configuration are read out independently, coincidence measurements can be made to discriminate neutrons [17], [22]–[24], [60]–[63]. Discrimination based on coincidence measurements will be discussed in more details later in this section.

Neutron discrimination can also be achieved by specifically designing the electrodes on the diamond detector. Alpha particles released from the converter and diamond interactions with

neutrons transverse only a few micrometers in diamond. Therefore, all created charge carriers are localized to a small region of a diamond as illustrated in Figure 3.1. Gamma radiation, on the other hand, interacts weakly with diamond and pass through the whole volume of the detector without losing too much energy and create charge carriers throughout the volume of the detector as illustrated on the right of Figure 3.3. By designing electrodes that can provide spatial information, ion interaction can be discriminated from photon interaction. However, the design on the electrodes also influences the detector capacitance which, as was discussed in the previous section, influences the SNR and can limit the system bandwidth.

5.3. Discrimination based on Pulse Shape Analysis

As mentioned above, ions and photons produce different ionization profiles since they interact with the diamond through different mechanisms. Photons produce charge carriers throughout the volume of the detector. These charge carriers start drifting to their respective electrodes at approximately the same time leading to an initial large induced current at the electrode which decreases linearly with time. As the charge reaches the electrode, they stop moving and therefore stop inducing current in the electrode. The charge that was generated closes to the electrode stopes first, while the charge generated at the other end of the diamond must drift through the entire volume of the detector. Since the externally applied electric field is constant and the drift velocity of the charge carriers is constant, this leads to a triangular induced current profile as illustrated on the left of Figure 5.5 [64].

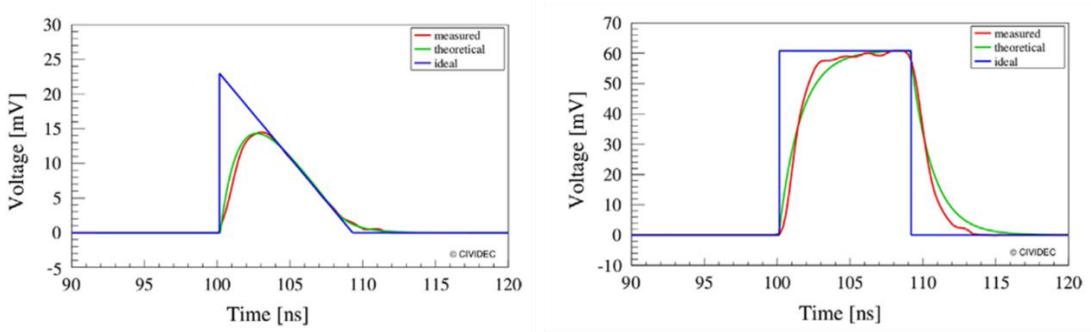

Figure 5.5 - Pulses generated by Gamma Radiation and Alpha Particles

Ions, such as the alpha particles emitted from nuclear reactions with neutrons do not have enough energy to pass through the whole volume of the detector and transfer all their energy to the

diamond in a few micrometers. Since most of the generated electron hole pairs are concentrated at one location, the induced current profile follows more of a rectangular shape as illustrated in Figure 3.1 and on the right of Figure 5.5. Using the TCT method, the general induced current profile can be detected with slight deviations from the theoretical shape due to the RC time constant of the system.

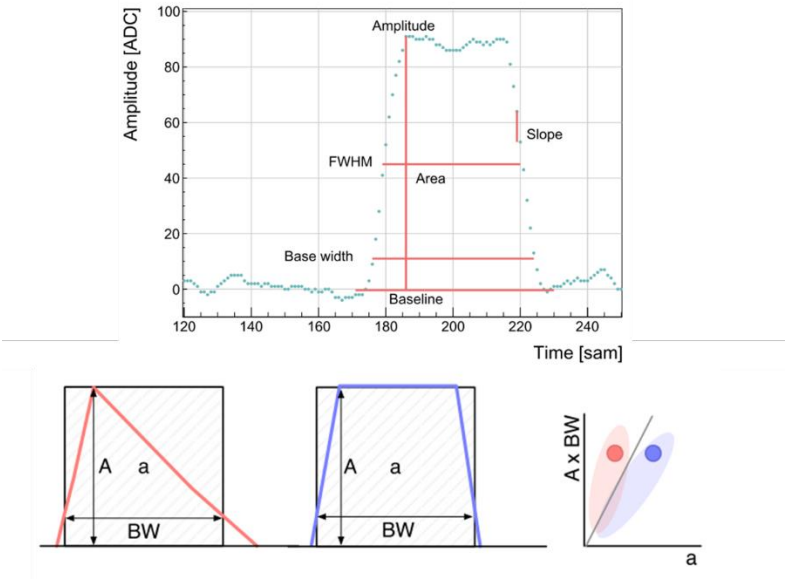

Figure 5.6 - Pulse shape discrimination parameters

Algorithms have been developed to analyze the base width, amplitude, area and slope of each pulse and discriminate neutrons from gamma radiation based on two or more of these parameters as show in Figure 5.6 [36], [64]. However, TCT signals are obtained with a broadband amplifier without any further pulse processing to improve the signal to noise ratio, this method is very sensitive to noise which can dramatically alter the shape of the pulse. Furthermore, fast neutrons can generate neutrons anywhere in the volume of the diamond detector which will also influence the induced current profile. As can be observed from the 3D plot of Figure 5.7, the induced current profile varies as a function of where the alpha particle is created in the diamond volume. Only near the electrode and in the ballistic center of the diamond detector will the induced current pulse be completely rectangular. At all other positions, the current profile will have a large initial peak and then a rectangular pulse as illustrated on the right of Figure 5.7 [64]. This technique has been applied to discriminate neutrons from photons with a diamond detector, however only at room

temperature. As discussed earlier, the CCE of a diamond detector drops significantly at low temperatures resulting in the TCT pulse amplitude to be 20 % of the room temperature value. This significantly degrades the signal to noise ratio and makes discrimination based on current pulse shape very difficult.

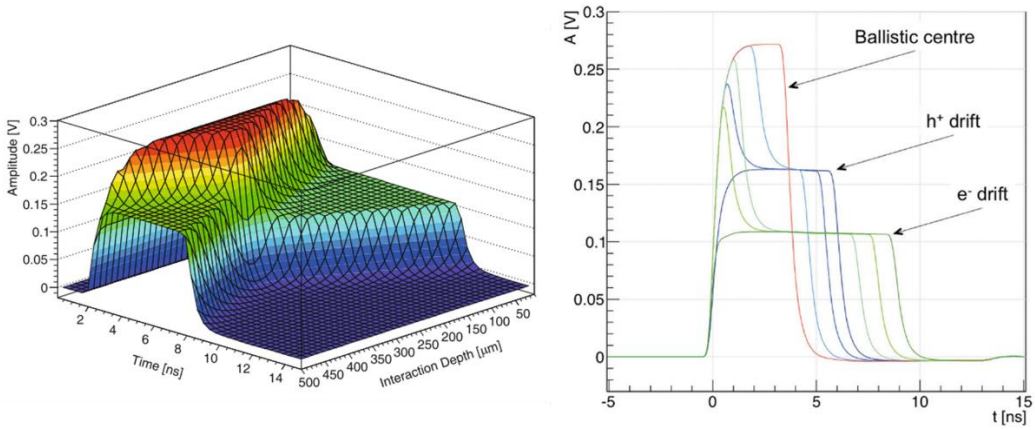

Figure 5.7 - Alpha particle current profile vs generation depth in a diamond detector

Pulse shape discrimination can also be performed using a charge sensitive preamplifier since the difference induced current profiles will influence the rise and fall time of the integrated current pulse. Although a lot of signal information is lost due to the bandwidth limits of the charge sensitive preamplifier. The most common way of performing such discrimination is by utilizing the zero-crossing method. If the zero-pole correction is not applied to the output of a charge sensitive preamplifier or a bipolar shaper is used, the resulting signal will cross the baseline voltage level. Different rise and fall times will result in this zero-crossing point to occur at different times relative to the rising edge of the pulse. Discrimination can be performed by comparing the time between the leading edge of the signal and the zero-crossing point for various signals.

Such methods are widely applied to neutron-gamma discrimination in scintillator based detector systems. As with diamond detectors, particles and photons are detected through different mechanisms which produce difference pulse shapes at the output of the detector. In scintillator based detectors, the length of the signal pulse is much larger resulting in an observable difference in the output of a charge integrating preamplifier as illustrated in Figure 5.8.

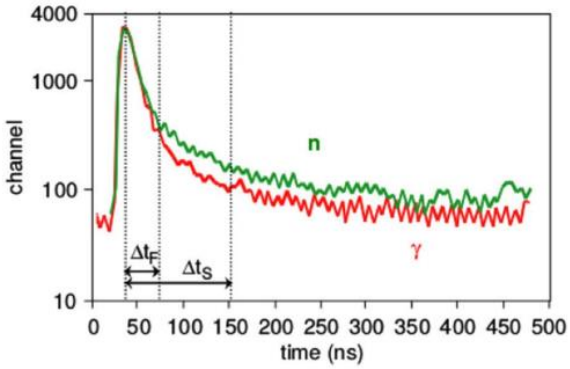

Figure 5.8 - Output signals of neutron and gamma radiation from a scintillator detector coupled to a charge sensitive preamplifier [65]

Signals presented in Figure 5.8 are successfully discriminated by comparing the integral of the signals over two intervals. This method is one of the few discrimination techniques which were implemented to run on FPGAs in real time [66]–[68]. Another method which was also implemented to run in real time is based on measuring the similarity of two vectors by calculating the cosine of the angle between them. Mathematically this is expressed as:

$$\cos\theta = \frac{x \cdot y}{|x||y|} = \frac{\sum_i^p x_i y_i}{\sqrt{\sum_i^p x_i^2}\sqrt{\sum_i^p y_i^2}} \tag{6.1}$$

where the input pulse x is compared to a template pulse y over p number of points and discrimination can be performed based on the cosine of the angle between the two pulse. This method can be further simplified replacing the template function with a unit step function and only comparing a portion of the signal, such as the rising edge of the signal. In this case the equation simplifies to [69]:

$$\cos\theta = \frac{\sum_i^p x_i}{\sqrt{p}\sqrt{\sum_i^p x_i^2}} \tag{6.2}$$

The above presented methods are easier to implement and provide pulse shape discrimination for signals from a scintillator detector, however these methods are not 100 % efficient and the discrimination criteria has to be set manually. Due to these shortfalls, these methods are not reliable

enough for radiation rate measurements in applications such as machine control and safety. Advance techniques utilizing machine learning and artificial neural networks are being applied to pulse shape discrimination to develop a more robust and reliable system [65], [70], [71].

Furthermore, the same problem of neutron gamma discrimination also exists in ^{3}He neutron detectors. Advanced discrimination techniques such as Linear Discriminant Analysis and Multivariate Analysis were successfully applied both offline and in real time to signals from this type of detector to separate neutrons from gamma events [72].

5.4. Discrimination based of event coincidences

As mentioned above, a detector layout can be chosen to allow for discrimination based on the coincidence of two signals in time. One example of this is with the sandwich detector layout where signals from one detector are compared to signals from the other and expected neutron reactions are discriminated by setting a coincidence time window.

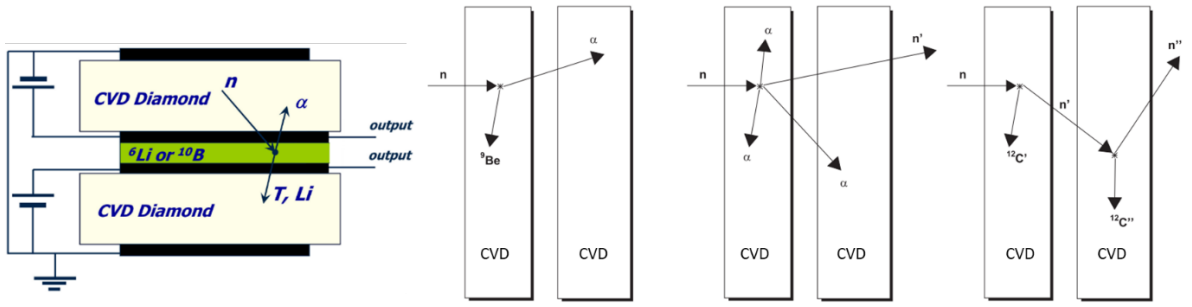

Figure 5.9 - Coincidence discrimination based on nuclear reaction products

Figure 5.9 illustrated a sandwich detector with possible strategies for detecting only neutrons. The figure on the left shows the reactions ^{6}Li(n,α)^{3}H and ^{10}B(n,α)^{7}Li for slow neutrons. Neutrons can be discriminated by only accepting events where both products of the reaction are detected. If the output of the top and bottom CVD diamond detectors are combined, the energy from both reaction products will be detected resulting in a peak in the spectrum at higher energy, allowing for discrimination based on energy as well [17]. The figure on the right of Figure 5.9 illustrates possible reaction for fast neutrons, specifically ^{12}C(n,α)^{9}Be, ^{12}C(n,n$'$)3α and ^{12}C(n,n$'$)^{12}C* reaction where * denotes an excited state. Neutrons can be discriminated by looking for events where only the specific coincidence of signals occur [63].

6. CONCLUSION

Recent advances in accelerator and fusion technology requires new generation of detectors that will be able to meet the requirements of operating in harsh environments reliably. Detectors based on single crystal CVD diamond are seen as one possible solution that could meet these requirements. As a wide bandgap semiconductor (5.47 eV), with high mobility of charge carriers, diamond allows for a large bias potential to be applied with a very low leakage current, thus making it suitable for a high dynamic range operation from very low to very high rate measurements. Furthermore, due to its large atomic displacement energy (43 eV), it is intrinsically radiation hard and therefore it can be placed close to the high intensity radiation sources found in accelerators. Due to these characteristics and their compact size, scCVD diamond detectors are prime candidates for BLM in large accelerator facilities such as the LHC, IFMIF-DONES and ITER. However, due to the use of superconducting magnets in these facilities, detectors that are places close to the beam or plasma source must also operate at cryogenic temperatures. As presented, scientific literature in this field is very scares and there exists an opportunity to contribute significantly, not only theoretically, but practically as well to the construction of future fusion devices such as DONES and ITER as well as general nuclear physics research facilities such as CERN.

This work provides and insight into the various aspects of detector development and the current state of the art technology level of diamond detectors. Focus was given to the operation of a diamond detector at cryogenic temperatures and the problems that arise from utilizing a detector in such an environment. Furthermore, a background of neutron detectors was given with different strategies that exist for the discrimination of neutrons from a gamma background. Many of the concept presented have not been applied at cryogenic temperatures, let alone to a diamond detector, prompting the need for further investigations. Different digital filtering techniques will need to be developed that work in conjunction with pulse shape analysis algorithm in order to extract useful information. Signal processing techniques have to be exploited to extract useful information from the detector since the signal to noise ratio at cryogenic temperatures decreases drastically. Therefore, it is crucial to study the individual noise sources and noise characteristics to improve the signal to noise ratio through signal processing.

The development of a cryogenic diamond based neutron detector that can operate reliably has many benefits over traditional detectors and can help further research in achieving the ultimate goal of sustainable nuclear fusion for producing electricity.

REFERENCES

[1] A. J. H. Donné, “The European roadmap towards fusion electricity,” *Philos. Trans. R. Soc. A Math. Phys. Eng. Sci.*, vol. 377, no. 2141, 2019, doi: 10.1098/rsta.2017.0432.

[2] J. M. Arroyo *et al.*, “Dones conceptual design report,” no. April, 2014.

[3] J. Egberts, “IFMIF-LIPAc Beam Diagnostics: Profiling and Loss Monitoring Systems,” Universite Paris Sud, 2012.

[4] J. Marroncle, P. Abbon, J. Egberts, and M. Pomorsk, “u-loss detector for Ifmif-Eveda,” *Proc. DIPAC2011*, pp. 146–148, 2008.

[5] J. Marroncle, P. Abbon, A. Marchix, and M. Pomorski, “R & D on micro-loss monitors for high intensity LINACS like LIPAc,” *Beam Instruments Interact.*, pp. 538–542, 2016.

[6] W. De Boer *et al.*, “Radiation hardness of diamond and silicon sensors compared,” *Phys. Status Solidi Appl. Mater. Sci.*, vol. 204, no. 9, pp. 3004–3010, 2007, doi: 10.1002/pssa.200776327.

[7] F. Bachmair, “Diamond sensors for future high energy experiments,” *Nucl. Instruments Methods Phys. Res. Sect. A Accel. Spectrometers, Detect. Assoc. Equip.*, vol. 831, pp. 370–377, Sep. 2016, doi: 10.1016/j.nima.2016.03.039.

[8] W. Adam *et al.*, “Radiation hard diamond sensors for future tracking applications,” *Nucl. Instruments Methods Phys. Res. Sect. A Accel. Spectrometers, Detect. Assoc. Equip.*, vol. 565, no. 1, pp. 278–283, Sep. 2006, doi: 10.1016/j.nima.2006.05.127.

[9] H. Kagan *et al.*, “Diamond detector technology, status and perspectives,” *Nucl. Instruments Methods Phys. Res. Sect. A Accel. Spectrometers, Detect. Assoc. Equip.*, vol. 924, pp. 297–300, 2018, doi: 10.1016/j.nima.2018.06.009.

[10] I. Zamboni, Ž. Pastuović, and M. Jakšić, “Radiation hardness of single crystal CVD diamond detector tested with MeV energy ions,” *Diam. Relat. Mater.*, 2013, doi: 10.1016/j.diamond.2012.11.002.

[11] R. S. Sussmann, *CVD Diamond for Electronic Devices and Sensors*. Chichester, UK: John Wiley & Sons, Ltd, 2009.

[12] J. K. Shultis and R. E. Faw, *Radiation shielding*. La Grange Park, IL: American Nuclear Society, 2000.

[13] J. Beringer *et al.*, “Review of particle physics,” *Phys. Rev. D - Part. Fields, Gravit. Cosmol.*, vol. 86, no. 1, 2012, doi: 10.1103/PhysRevD.86.010001.

[14] G. F. Knoll, *Radiation Detection and Measurement*, 4th ed. New York: John Wiley and Sons, Inc., 2010.

[15] J. F. Ziegler, M. D. Ziegler, and J. P. Biersack, “SRIM - The stopping and range of ions in matter (2010),” *Nucl. Instruments Methods Phys. Res. Sect. B Beam Interact. with Mater. Atoms*, vol. 268, no. 11–12, pp. 1818–1823, 2010, doi: 10.1016/j.nimb.2010.02.091.

[16] J. Lilley, *Nuclear Physics - Principles and Applications*. Wiley, 2001.

[17] M. Angelone and C. Verona, “Properties of Diamond-Based Neutron Detectors Operated in Harsh

Environments," *J. Nucl. Eng.*, vol. 2, no. 4, pp. 422–470, 2021, doi: 10.3390/jne2040032.

[18] "Experimental Nuclear Reaction Data (EXFOR)," *International Atomic Energy Agency*. https://www-nds.iaea.org/exfor/ (accessed Mar. 11, 2022).

[19] "NuDat 3.0," *National Nuclear Data Center*. https://www.nndc.bnl.gov/nudat3/ (accessed Mar. 11, 2022).

[20] C. Weiss, H. Frais-Kölbl, E. Griesmayer, and P. Kavrigin, "Ionization signals from diamond detectors in fast-neutron fields," *Eur. Phys. J. A*, vol. 52, no. 9, Sep. 2016, doi: 10.1140/epja/i2016-16269-8.

[21] W. Catford, "CATKIN." http://personal.ph.surrey.ac.uk/~phs1wc/kinematics/ (accessed Mar. 17, 2022).

[22] M. Angelone *et al.*, "Neutron detectors based upon artificial single crystal diamond," *IEEE Trans. Nucl. Sci.*, vol. 56, no. 4, pp. 2275–2279, 2009, doi: 10.1109/TNS.2009.2025177.

[23] M. Osipenko *et al.*, "Neutron spectrometer for fast nuclear reactors," *Nucl. Instruments Methods Phys. Res. Sect. A Accel. Spectrometers, Detect. Assoc. Equip.*, vol. 799, pp. 207–213, Nov. 2015, doi: 10.1016/j.nima.2015.07.050.

[24] J. Holmes *et al.*, "Performance of 5-μm PIN diamond diodes as thermal neutron detectors," *Nucl. Instruments Methods Phys. Res. Sect. A Accel. Spectrometers, Detect. Assoc. Equip.*, vol. 961, no. December 2019, p. 163601, 2020, doi: 10.1016/j.nima.2020.163601.

[25] X. Xie *et al.*, "Application of a single crystal chemical vapor deposition diamond detector for deuteron plasma neutron measurement," *Nucl. Instruments Methods Phys. Res. Sect. A Accel. Spectrometers, Detect. Assoc. Equip.*, vol. 761, pp. 28–33, Oct. 2014, doi: 10.1016/j.nima.2014.05.067.

[26] H. Barschall *et al.*, *Neutron sources for basic physics, and their applications*, 1st ed. Oxford; New York: Pergamon Press, 1983.

[27] S. Friedland S., J. Mayer, W., and J. Wiggins, S., "The solid ionization chamber," *IRE Trans. Nucl. Sci.*, vol. 7, no. 2/3, pp. 181–185, 1960, doi: 10.1109/TNS2.1960.4315761.

[28] C. Weiss, "A CVD Diamond Detector for (n,α) Cross-Section Measurements," Vienna University of Technology, Vienna, 2014.

[29] M. Pomorski, "Electronic properties of single crystal CVD diamond and its suitability for particle detection in hardron physics experiments," no. January 2008, 2008.

[30] H. Jansen, "Chemical Vapour Deposition Diamond - Charge Carrier Movement at Low Temperatures and Use in Time-Critical Applications," Bonn University, 2013.

[31] D. Jain, J. Nuwad, N. Manoj, and V. Sudarsan, "Diamond-Based Radiation Detectors for Applications in Highly Corrosive Solutions and High-Radiation Fields," in *Materials Under Extreme Conditions: Recent Trends and Future Prospects*, Elsevier Inc., 2017, pp. 683–715.

[32] R. Alig, C., S. Bloom, and C. Struck, W., "Scattering by ionization and phonon emission in semiconductors," *Phys. Rev. B*, vol. 22, no. 12, pp. 5565–5582, 1980, doi: 10.1103/physrevb.22.5565.

[33] H. Pernegger *et al.*, "Charge-carrier properties in synthetic single-crystal diamond measured with

the transient-current technique," *J. Appl. Phys.*, vol. 97, no. 7, 2005, doi: 10.1063/1.1863417.

[34] S. Ramo, "Currents Induced by Electron Motion," *Proc. od IRE*, vol. 27, no. 9, 1939.

[35] H. Pernegger, "High mobility diamonds and particle detectors," *Phys. Status Solidi Appl. Mater. Sci.*, vol. 203, no. 13, pp. 3299–3314, 2006, doi: 10.1002/pssa.200671404.

[36] M. Cerv, "CVD diamond applications for particle detection and identification in high-radiation environments," Technical University Vienna, Vienna, 2016.

[37] S. M. Sze and K. K. Ng, *Physics of Semiconductor Devices*, 3rd ed. Hoboken, NJ, USA: John Wiley & Sons, Inc., 2006.

[38] M. A. Tamor and J. P. Wolfe, "Drift and diffusion of free excitons in Si," *Phys. Rev. Lett.*, vol. 44, no. 25, pp. 1703–1706, 1980, doi: 10.1103/PhysRevLett.44.1703.

[39] P. J. Dean, E. C. Lightowlers, and D. R. Wight, "Intrinsic and extrinsic recombination radiation from natural and synthetic aluminum-doped diamond," *Phys. Rev.*, vol. 140, no. 1A, 1965, doi: 10.1103/PhysRev.140.A352.

[40] H. Jansen, D. Dobos, T. Eisel, H. Pernegger, V. Eremin, and N. Wermes, "Temperature dependence of charge carrier mobility in single-crystal chemical vapour deposition diamond," *J. Appl. Phys.*, vol. 113, no. 17, 2013, doi: 10.1063/1.4802679.

[41] H. Jansen, D. Dobos, H. Pernegger, N. Wermes, V. Eremin, and R. Sauer, "C-TCT measurements on scCVD diamond and its use at CNGS." DESY, Hamburg, pp. 1–47, 2014.

[42] M. Guthoff, "Radiation Damage to the diamond-based Beam Condition Monitor of the CMS Detector at the LHC," p. 173, 2014, [Online]. Available: https://cds.cern.ch/record/1977429?ln=de.

[43] T. Naaranoja, M. Golovleva, L. Martikainen, M. Berretti, and K. Österberg, "Space charge polarization in irradiated single crystal CVD diamond," *Diam. Relat. Mater.*, vol. 96, pp. 167–175, Jun. 2019, doi: 10.1016/j.diamond.2019.03.007.

[44] M. R. Ramos, A. Crnjac, D. Cosic, and M. Jakši, "Ion Microprobe Study of the Polarization Quenching Techniques in Single Crystal Diamond Radiation Detectors," *Materials (Basel).*, vol. 15, no. 1, p. 388, 2022, doi: https://doi.org/10.3390/ma15010388.

[45] F. Nava *et al.*, "Transport properties of natural diamond used as nuclear particle detector for a wide temperature range," *IEEE Trans. Nucl. Sci.*, vol. NS-26, no. 1, 1979.

[46] J. Isberg, M. Gabrysch, S. Majdi, and D. J. Twitchen, "Negative electron mobility in diamond," *Appl. Phys. Lett.*, vol. 100, no. 17, 2012, doi: 10.1063/1.4705434.

[47] K. Konishi, I. Akimoto, J. Isberg, and N. Naka, "Diffusion-related lifetime and quantum efficiency of excitons in diamond," *Phys. Rev. B*, vol. 102, no. 19, p. 195204, 2020, doi: 10.1103/PhysRevB.102.195204.

[48] T. Ichii, Y. Hazama, N. Naka, and K. Tanaka, "Study of detailed balance between excitons and free carriers in diamond using broadband terahertz time-domain spectroscopy," *Appl. Phys. Lett.*, vol. 116, no. 23, p. 231102, 2020, doi: 10.1063/5.0006993.

[49] J. Marroncle *et al.*, "IFMIF-LIPAC diagnostics and its challenges," *IBIC 2012 - Proc. 1st Int. Beam*

Instrum. Conf., pp. 557–565, 2013.

[50] J. Scherzinger *et al.*, "Tagging fast neutrons from a 252Cf fission-fragment source," *Appl. Radiat. Isot.*, vol. 128, no. December 2016, pp. 270–274, 2017, doi: 10.1016/j.apradiso.2017.05.022.

[51] D. Cosic, M. Bogovac, and M. Jakšić, "Data acquisition and control system for an evolving nuclear microprobe," *Nucl. Instruments Methods Phys. Res. Sect. B Beam Interact. with Mater. Atoms*, 2019, doi: 10.1016/j.nimb.2019.05.047.

[52] D. Cosic, G. Provatas, M. Jakšić, and D. Begušić, "Charge collection efficiency of scCVD diamond detectors at low temperatures," *Diam. Relat. Mater.*, vol. 127, no. March, p. 109184, Aug. 2022, doi: 10.1016/j.diamond.2022.109184.

[53] M. Nakhostin, "Signal Processing for Radiation Detectors," p. 528, Oct. 2017, doi: 10.1002/9781119410225.

[54] H. Spieler, *Semiconductor Detector Systems*. Oxford University Press, 2005.

[55] P. W. Nicholson, *Nuclear Electronics*. Hoboken, NJ, USA: John Wiley & Sons, Inc., 1974.

[56] Z. Guzik and T. Krakowski, "Algorithms for digital gamma-ray spectroscopy," *Nukleonika*, vol. 58, no. November 2012, pp. 333–338, 2013.

[57] V. T. Jordanov, G. F. Knoll, A. C. Huber, and J. A. Pantazis, "Digital techniques for real-time pulse shaping in radiation measurements," *Nucl. Inst. Methods Phys. Res. A*, vol. 353, no. 1–3, pp. 261–264, 1994, doi: 10.1016/0168-9002(94)91652-7.

[58] E. Vittone, "Theory of ion beam induced charge measurement in semiconductor devices based on the Gunn's theorem," in *Nuclear Instruments and Methods in Physics Research, Section B: Beam Interactions with Materials and Atoms*, Jun. 2004, vol. 219–220, no. 1–4, pp. 1043–1050, doi: 10.1016/j.nimb.2004.01.210.

[59] M. Pillon, M. Angelone, A. Krása, A. J. M. Plompen, P. Schillebeeckx, and M. L. Sergi, "Experimental response functions of a single-crystal diamond detector for 5–20.5MeV neutrons," *Nucl. Instruments Methods Phys. Res. Sect. A Accel. Spectrometers, Detect. Assoc. Equip.*, vol. 640, no. 1, pp. 185–191, Jun. 2011, doi: 10.1016/j.nima.2011.03.005.

[60] S. Almaviva *et al.*, "Improved performance in synthetic diamond neutron detectors: Application to boron neutron capture therapy," *Nucl. Instruments Methods Phys. Res. Sect. A Accel. Spectrometers, Detect. Assoc. Equip.*, vol. 612, no. 3, pp. 580–582, 2010, doi: 10.1016/j.nima.2009.08.016.

[61] M. Marinelli *et al.*, "High performance 6Li F -diamond thermal neutron detectors," *Appl. Phys. Lett.*, vol. 89, no. 14, 2006, doi: 10.1063/1.2356993.

[62] M. Osipenko *et al.*, "Calibration of a 6Li diamond-sandwich spectrometer with quasi-monoenergetic neutrons," *Nucl. Instruments Methods Phys. Res. Sect. A Accel. Spectrometers, Detect. Assoc. Equip.*, vol. 931, pp. 135–141, Jul. 2019, doi: 10.1016/j.nima.2019.04.015.

[63] M. Osipenko *et al.*, "Response of a diamond detector sandwich to 14 MeV neutrons," *Nucl. Instruments Methods Phys. Res. Sect. A Accel. Spectrometers, Detect. Assoc. Equip.*, vol. 817, pp. 19–25, May 2016, doi: 10.1016/j.nima.2016.02.008.

[64] P. Kavrigin, P. Finocchiaro, E. Griesmayer, E. Jericha, A. Pappalardo, and C. Weiss, "Pulse-shape

analysis for gamma background rejection in thermal neutron radiation using CVD diamond detectors," *Nucl. Instruments Methods Phys. Res. Sect. A Accel. Spectrometers, Detect. Assoc. Equip.*, 2015, doi: 10.1016/j.nima.2015.05.040.

[65] M. Astrain *et al.*, "Real-Time Implementation of the Neutron/Gamma Discrimination in an FPGA-Based DAQ MTCA Platform Using a Convolutional Neural Network," *IEEE Trans. Nucl. Sci.*, vol. 68, no. 8, pp. 2173–2178, Aug. 2021, doi: 10.1109/TNS.2021.3090670.

[66] M. Pavelek *et al.*, "Fast digital spectrometer for mixed radiation fields," in *2017 IEEE SENSORS*, Oct. 2017, pp. 1–3, doi: 10.1109/ICSENS.2017.8234012.

[67] T. Szczesmak *et al.*, "Digital neutron-gamma discrimination methods: Charge comparison versus zero-crossing," in *2014 IEEE Nuclear Science Symposium and Medical Imaging Conference (NSS/MIC)*, Nov. 2014, pp. 1–4, doi: 10.1109/NSSMIC.2014.7431222.

[68] M. Nakhostin, "Recursive algorithms for digital implementation of neutron/gamma discrimination in liquid scintillation detectors," *Nucl. Instruments Methods Phys. Res. Sect. A Accel. Spectrometers, Detect. Assoc. Equip.*, vol. 672, pp. 1–5, Apr. 2012, doi: 10.1016/j.nima.2011.12.113.

[69] M. Nakhostin, "A general-purpose digital pulse shape discrimination algorithm," *IEEE Trans. Nucl. Sci.*, vol. 66, no. 5, pp. 838–845, May 2019, doi: 10.1109/TNS.2019.2910153.

[70] T. S. Sanderson, C. D. Scott, M. Flaska, J. K. Polack, and S. A. Pozzi, "Machine learning for digital pulse shape discrimination," in *2012 IEEE Nuclear Science Symposium and Medical Imaging Conference Record (NSS/MIC)*, Oct. 2012, pp. 199–202, doi: 10.1109/NSSMIC.2012.6551092.

[71] C. Fu, A. Di Fulvio, S. D. Clarke, D. Wentzloff, S. A. Pozzi, and H. S. Kim, "Artificial neural network algorithms for pulse shape discrimination and recovery of piled-up pulses in organic scintillators," *Ann. Nucl. Energy*, vol. 120, pp. 410–421, Oct. 2018, doi: 10.1016/j.anucene.2018.05.054.

[72] C. L. Wang, L. L. Funk, R. A. Riedel, and K. D. Berry, "Improved neutron-gamma discrimination for a 3He neutron detector using subspace learning methods," *Nucl. Instruments Methods Phys. Res. Sect. A Accel. Spectrometers, Detect. Assoc. Equip.*, vol. 853, pp. 27–35, May 2017, doi: 10.1016/j.nima.2017.02.022.

LIST OF ABBREVIATIONS

AC	Alternating Current
ADC	Analog to Digital Converter
BLM	Beam Loss Monitor
CCD	Charge Collection Distance
CCE	Charge Collection Efficiency
CERN	European Organization for Nuclear Research
CVD	Chemical Vapor Deposition
DC	Direct Current
D-D	Deuterium – Deuterium
DEMO	Demonstration Power Plant
DONES	DEMO Oriented Neutron Source
EMI	Electromagnetic Interference
ENC	Noise Equivalent Charge
FEE	Front End Electronics
FIR	Finite Impulse Response
FPGA	Field Programmable Gate Array
FWHM	Full Width at Half Maximum
HTHP	High Temperature High Pressure
HWR	Half Wave Resonator
IAEA	International Atomic Energy Energy
IBA	Ion Beam Analysis
IBIC	Ion Beam Induced Charge
IFMIF	International Fusion Material Irradiation Facility

IIR	Infinite Impulse Response
ITER	International Thermonuclear Experimental Reactor
LHC	Large Hadron Collider
LIPAc	Linear IFMIF Prototype Accelerator
NDM	Negative Differential Mobility
NNDC	National Nuclear Data Center
PCB	Printed Circuit Board
pCVD	Polycrystalline Chemical Vapor Deposition
PHA	Pulse Height Analysis
RC	Resistor Capacitor
RMS	Root Mean Square
scCVD	Single Crystal Chemical Vapor Deposition
SNR	Single to Noise Ratio
SRIM	Stopping and Range of Ions in Matter
TCT	Transit Current Technique
T-D	Tritium – Deuterium

ABSTRACT

New generation of accelerators and fusion devices require advance detectors which can operate reliably at low temperature, in mixed radiation environments and under high radiation fluences. Detectors based on single crystal diamond are seen as one possible solution that could meet these requirements and have been proposed to be used as micro beam loss monitors in such devices. However more research and development are required to confirm that diamond based detectors can detect and discriminate neutron radiation from other forms of radiation at cryogenic temperatures.

This work outlines the current state of research for diamond detectors with a specific focus on low temperatures and neutron detection. Diamond detector have been successfully used to detect and discriminate neutrons from gamma radiation at room temperature. However, it has been observed that the charge collection efficiency of diamond detectors drastically decreases at cryogenic temperatures. A cryogenic diamond detect has been created and preliminary experiments have been performed for the first time at cryogenic temperatures in neutron fields. Further refinements to the setup as well as different signal processing strategies have been proposed in this work as possible contributions to the development of diamond based micro beam loss monitors.